

ACTA MATERIALIA TRANSYLVANICA

Material Sciences Publications

Volume 5, Issue 2



ERDÉLYI MÚZEUM-EGYESÜLET
Cluj-Napoca
2022

A folyóirat megjelenését támogatta a Magyar Tudományos Akadémia, a Bethlen Gábor Alapkezelő Zrt., a Communitas Alapítvány és az EME Műszaki Tudományok Szakosztálya / The publication of this magazine was supported by the Hungarian Academy of Sciences, by the Bethlen Gábor Fund, by the Communitas Foundation and by the TMS – Department of Engineering Sciences.



Főszerkesztő / Editor-in-Chief: Bitay Enikő

Nemzetközi Tanácsadó testület / International Editorial Advisory Board:

Prof. Biró László Péter, MTA Energiatudományi Kutatóközpont, Budapest, Magyarország
 Prof. emer. B. Nagy János, University of Namur, Namur, Belgium
 Prof. Czigány Tibor, Budapesti Műszaki és Gazdaságtudományi Egyetem, Budapest, Magyarország
 Prof. Diószegi Attila, Jönköping University, Jönköping, Svédország
 Dobránszky János, ELKH–BME Kompozittechnológiai Kutatócsoport, Budapest, Magyarország
 Prof. Dusza János, Institute of Materials Research of Slovak Academy of Sciences, Kassa, Szlovákia
 Prof. Kaptay György, Miskolci Egyetem, Miskolc, Magyarország
 Dr. Kolozsváry Zoltán, Plasmaterm Rt., Marosvásárhely, Románia
 Prof. Mertinger Valéria, Miskolci Egyetem, Miskolc, Magyarország
 Prof. Porkoláb Miklós, Massachusetts Institute of Technology, Cambridge, MA, USA
 Prof. Réger Mihály, Óbudai Egyetem, Budapest, Magyarország
 Prof. emer. Réti Tamás, Óbudai Egyetem, Budapest, Magyarország
 Prof. emer. Roósz András, Miskolci Egyetem, Miskolc, Magyarország
 Dr. Spenik Sándor, Ungvári Nemzeti Egyetem, Ungvár, Ukrajna
 Prof. Zsoldos Ibolya, Széchenyi István Egyetem, Győr, Magyarország

Lapszám szerkesztők / Editorial Board:

Dobránszky János, ELKH–BME Kompozittechnológiai Kutatócsoport, Budapest, Magyarország
 Csavdári Alexandra, Babeş–Bolyai Tudományegyetem, Kolozsvár, Románia
 Gergely Attila, Sapientia Erdélyi Magyar Tudományegyetem, Marosvásárhely, Románia
 Kovács Tünde, Óbudai Egyetem, Budapest, Magyarország

Kiadó / Publisher: Erdélyi Múzeum-Egyesület

Felelős kiadó / Responsible publisher: Biró Annamária

Olvasószerkesztő / Proofreader: Szenkovics Enikő (magyar), David Speight (English)

Szerkesztőségi titkár / Editorial secretary: Kisfaludi-Bak Zsombor

Borítótér / Cover: Kőnczey Elemér

Nyomdai munkálatok / Printed at: F&F International Kft., Gyergyószentmiklós

Copyright © a szerzők / the authors, EME/ TMS 2022

ISSN 2601-1883, ISSN-L 2601-1883

DOI: 10.33923/amt-2022-02

A folyóirat honlapja: <https://www.eme.ro/publication-hu/acta-mat/mat-main.htm>

The journal website: <https://www.eme.ro/publication/acta-mat/mat-main.htm>

Az Acta Materialia Transylvanica. Anyagtudományi Közlemények az Erdélyi Múzeum-Egyesület (EME) Műszaki Tudományok Szakosztályának folyóirata, amely az anyagtudományok területéről közlő tudományos közleményeket: szakcikkeket, összefoglalókat (szemléket), tanulmányokat. A folyóirat célja összképet adni kiemelten a Kárpát-medencei kutatási irányokról, tudományos eredményeiről, s ezt széles körben terjeszteni is. A folyóirat az EME felvállalt céljaihoz híven a magyar szaknyelv ápolását is támogatja, így a nyomtatott folyóirat magyar nyelven jelenik meg, mely az Erdélyi digitális adattárban elérhető (<https://eda.eme.ro/handle/10598/30356>). A széles körű nemzetközi terjesztés érdekében a folyóirat teljes angol nyelvű változatát is közzétesszük.

Acta Materialia Transylvanica – Material Sciences Publications – is a journal of the Technical Sciences Department of the Transylvanian Museum Society, publishing scientific papers, issues, reviews and studies in the field of material sciences. Its mission is to provide and disseminate a comprehensive picture focusing on research trends and scientific results in the Carpathian basin. In accordance with the general mission of the Transylvanian Museum Society it aims to support specialized literature in Hungarian. The printed version of the journal is published in Hungarian and is available in the Transylvanian Digital Database (<https://eda.eme.ro/handle/10598/30356>). However, we would like to spread it internationally, therefore the full content of the journal will also be available in English.

Tartalom / Content

BAGYINSZKI Gyula.....	53
<i>Fémalapú habok jellemzői és vizsgálati szempontjai</i>	
<i>Characteristics and Test Aspects of Metal-Based Foams</i>	
BORHY Levente, LEVELES Borbála, KEMÉNY Alexandra.....	58
<i>A ragasztóanyag kiválasztása mikroszakító kötőszilárdsági vizsgálatokhoz</i>	
<i>Choosing the Adhesive for Microtensile Bond Strength Tests</i>	
FÁBIÁN Hunor, GERGELY Attila.....	62
<i>Nagy teljesítményű szálképző berendezés tervezése</i>	
<i>Design of a High Performance Fiber-producing Machine</i>	
FEKETE Gusztáv, TEJ Singh, JÁNOSI Endre.....	66
<i>Térdimplantátumok kopásának modellezése</i>	
<i>Wear Modelling of Total Knee Replacements</i>	
MESZLÉNYI György, BITAY Enikő	72
<i>Szállézeres sugármenetének elemzése a nyálábvezető optikai szál végétől a fókuszfoltig</i>	
<i>Analysis of Fibre Laser's Optical Construction from the End of the Beam Guiding Optical Fibre to the Focal Spot</i>	
MIHÁLY Norbert-Botond, CSAVDÁRI Alexandra	78
<i>Mesterséges neurális hálózatok alkalmazása adszorpciós vizsgálatokban. Esettanulmány</i>	
<i>Application of Artificial Neural Networks in Adsorption Studies. A case study</i>	
NAGY Gábor Zoltán, LÁZÁR Nikoletta, NAGY Roland	83
<i>Kézzetnövényolaj-alapú kenőanyag-adalékok alapanyagainak vizsgálata</i>	
<i>Investigation of Raw Materials for Sulfurized Vegetable Oil Based Lubricant Additives</i>	
SCHRAMKÓ Márton, KAFI Abdallah, KOVÁCS Tünde Anna	89
<i>A hegesztés során képződő UV-sugárzás egészségkárosító hatásának elemzése</i>	
<i>Analysis of the Harmful Effects of UV Radiation Generated During Welding</i>	

TRAUTMAN Bence, TÓTH László, FÁBIÁN Enikő Réka	93
<i>Csőperemezéshez használt szerszámacélok összehasonlítása</i>	
<i>Comparison of Tool Steels for Tube End Flanging</i>	
WINDISCH Márk, MALOVECZKY Anna, ARADI László, VERES Miklós, FÜRJES Péter, VIDA Ádám	99
<i>Lézerrel létrehozott periodikus felületi struktúrák (LIPSS) alkalmazásorientált felhasználása</i>	
<i>Application-oriented Use of Laser-induced Periodic Surface Structures</i>	

Characteristics and Test Aspects of Metal-Based Foams

Gyula BAGYINSZKI

Óbuda University, Bánki Donát Faculty of Mechanical and Safety Engineering, Budapest, Hungary,
 bagyinszki.gyula@bgk.uni-obuda.hu

Abstract

There is a continuous development in automotive body production to expand the use of metal foams. The use of aluminium foams in vehicles is made possible by the high strength/mass ratio, which means that mass reduction is not accompanied by a reduction in safety. Reducing mass (self-weight), on the other hand, is essential due to increasingly stringent environmental regulations. The present composition draws attention to the structural properties of metal-based foams and its testability.

Keywords: metal foam, cavity, sandwich structure, non-destructive testing, computed tomography.

1. Introduction

The group of „hybrids” included in a possible division scheme of structural materials (Figure 1) includes composites, sandwich structures - as a special subgroup of layered composites -, segmented (connected, bundled) structures and cellular materials of various designs, foams (Figure 2) [1]. Segmented (connected, bundled) material

structures are built from discrete units that can absorb significant loads as a block unit, while being sufficiently resistant to damage.

Among the porous materials, plastic foams are the most well-known: polystyrene foams („hungarocell”), polyurethane (PUR) foams, artificial sponges, packaging materials, etc. However, their applicability is limited by, among other things,

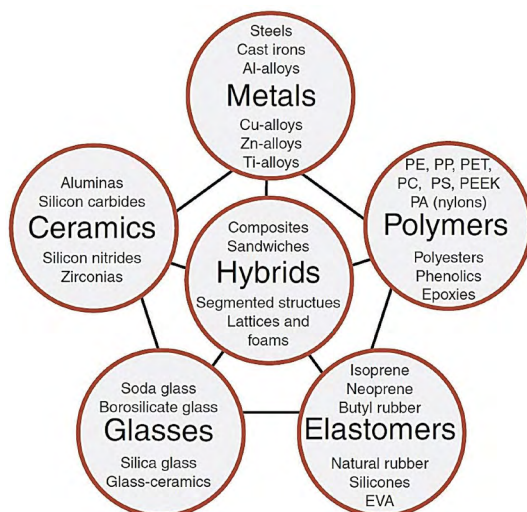


Figure 1. A possible division of structural materials and typical examples.

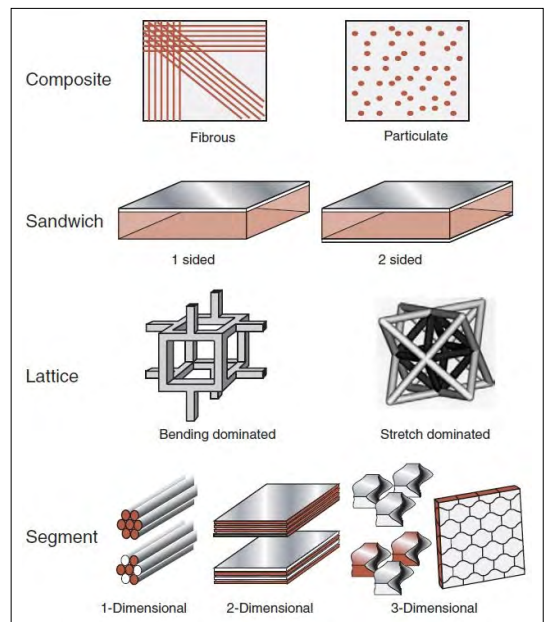


Figure 2. Subgroups of hybrid structural materials.

the strong temperature dependence of their properties and their inherently low strength [2]. In the case of metal foams, these disadvantages do not occur or occur to a lesser extent. Metal foams are lightweight cellular materials inspired by nature (biomimetics): e.g. cork, balsa wood, sponge, cancellous bone, coral, cuttle-bone and palm plant stalk also have a similar structure (Figure 3) [1].

2. Characteristics of metal-based foams

Based on their structure, metal foams can be divided into two groups (Figure 4) [3]:

- Open-cell metal foams, the cavities of which are connected to each other, and the framework of which is formed by interconnected cell edges;

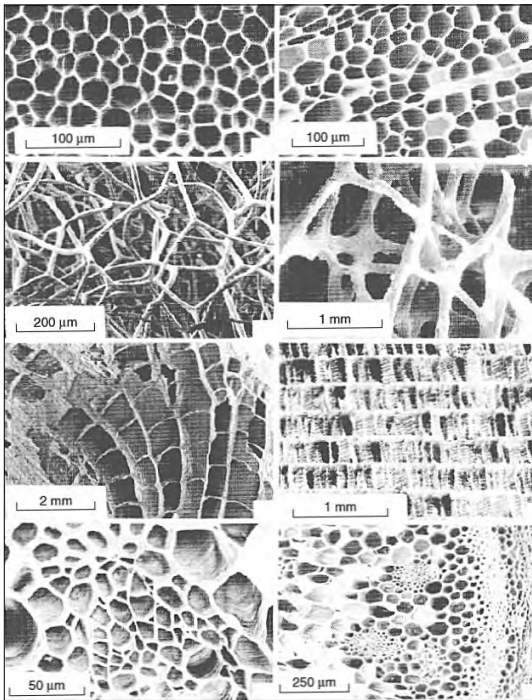


Figure 3. Cellular biostructures.

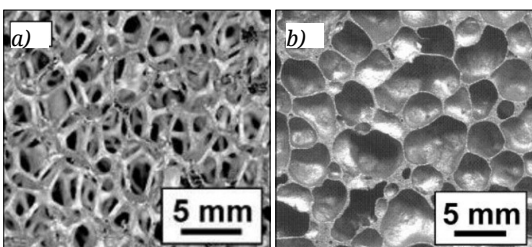


Figure 4. Open and closed cell metal foam.

- Closed-cell metal foams in which the cavities are separated by cell walls.

In order to (more) accurately identify metal foams, a distinction can be made between the materials (variants) commonly known as metal foam [4]:

- Cellular metals: the most general term that refers to a metal body in which cavities filled with gas can be found, i.e. the metal phase divides the material into cells, in which there is a gas phase.
- Porous metals: a special type of cellular metals, which are characterized by a kind of cavity, so the pores are usually round and separated from each other.
- Solid metal foams: A special class of cellular metals, which are formed from liquid metal foams and thus have a defined morphology. The cells are closed, round or polyhedral and separated by a thin layer of metal.
- Metal sponges: a morphological type of cellular metals in which there are open cells.

Figure 5 shows the division of cellular metals in terms of production technology [5].

Metal foams can contain cavities of a few micrometers or even centimeters in size, and the wall thickness of the cells in them can vary widely, while their structure is similar to plastic foams. The density of metal foams is significantly lower compared to that of solid metals, their average density can be up to one hundredth of the density of the metal. One of the most common characteristics of metal foams is the relative density, which is the ratio of the density of the metal foam to the density of the metal forming the metal foam, often given as a percentage. The relative density of currently produced metal foams varies between 0.1% and 50%. Solid metal foams are known for their combination of specific physical and mechanical properties, such properties are relatively high stiffness, low specific weight (density), relatively high compressive strength and good energy absorption [6].

Figure 6. summarizes the mixture states that can be formed from materials with characteristic states, including foam materials. In these heterogeneous (consisting of different parts) material mixtures, one material quality (or state of matter) is present in a larger (dominant) proportion, while the other - in a fine and uniform (dispersed) distribution - is present to a lesser extent [7].

The metal foams used are mostly aluminum-based and can be achieved with special production technology to create closed cavities in the

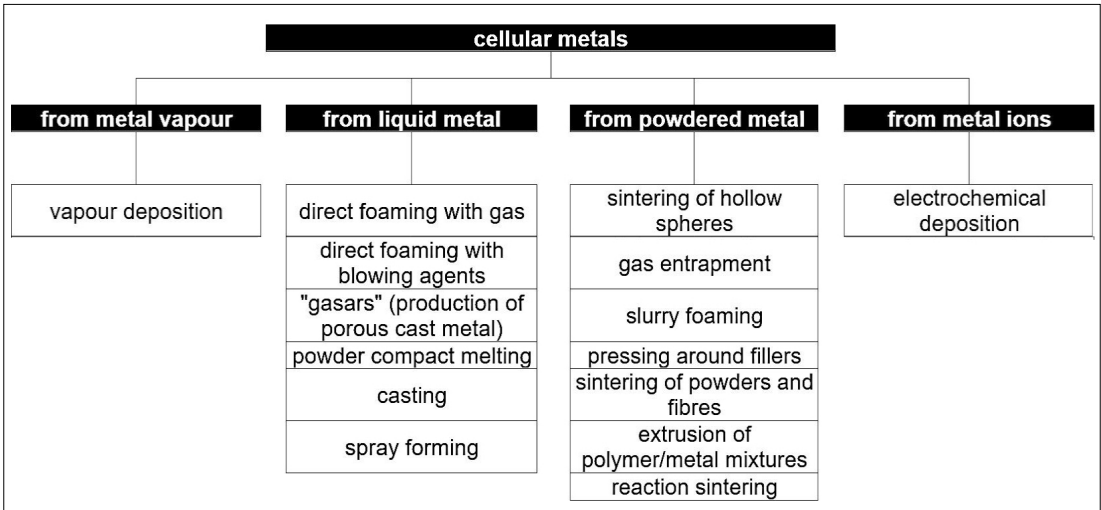


Figure 5. Division of cellular metals based on production technology.

Established mixture states, when		Material that we disperse		
		Gas	Liquid	Solid
Material in which we disperse	Gas	Gas mixture	Fog	Smoke
	Liquid	Foam	Emulsion	Suspension slurry
	Solid	Solid foam, cellular solid	Sludge Gel	Powder mixture Embedded particles

Figure 6. Foam materials between mixing states.

aluminum, thus giving the material a „spongy” structure. Components are produced in a closed mold, in which case the cavities of the foam are closed in contact with the surface of the mold, so the surface will be smooth and continuous. Another application is pouring thin-walled steel pipes with foamed metal. Since metal foams have good energy absorption and vibration damping capabilities, they are also excellent for stiffening pipes [8].

It is also possible to make sandwich structures using metal foams. Due to their advantageous properties, they can be used during body construction to stiffen support pillars, make floors and form bumpers. Due to their large specific surface area, they can also function as a support material for catalysts and as a large surface area electrode in batteries. Their electrical conductivity is lower than that of traditional metals.

When foaming with gas enclosed in pores, the high-pressure inert gas is trapped in the pores of the metal powder, so the metal powder is placed in a high-pressure gas space. Afterwards, this metal-gas mixture is rolled into a plate, while the wall of the sealed plate chamber forms solid side plates. The plate is heated so that the gas in the metal powder layer expands. With this method, a specific sandwich structure is obtained, i.e. a kind of composite, the core of which has a porosity of approximately 30%.

As an innovative material, aluminum foam has great potential for use as a composite component. It is a composite aluminum foam sandwich, which consists of aluminum plates as cover layers and aluminum foam as a core layer. Both the aluminum foam and the sandwich structure are completely recyclable and environmentally friendly, as they are made entirely of aluminum. These properties can be used very well for the bodywork of motor vehicles. In addition, the construction industry, the aerospace industry, marine and railway vehicle production also represent a great application potential.

3. Non-destructive material testing of metal-based foams

Continuity gaps must be detected using suitable test methods, with which they can either be recognized directly, or their presence can be inferred from some sign. The individual tests differ both in method and in the information content that can be obtained.

It is fundamentally important to keep in mind that there is no universal material testing method. Each method can only reliably detect discontinuities of a certain type and/or location, i.e. the individual non-destructive testing methods do not replace each other, but complement each other. Therefore, in some cases, a complex examination, i.e. the parallel execution of several methods, may be necessary.

The most important industrially applied non-destructive testing procedures:

- examination of density and physical (thermal, electrical, magnetic, optical, acoustic) properties,
- visual testing (VT),
- leak test (LT),
- penetrant testing (PT),
- magnetic particle testing (MT),
- eddy current testing (ET),
- ultrasonic testing (UT),
- radiographic testing (RT).

Various technical and economic requirements are imposed on the test methods, and the nature of the task is primarily decisive in selecting the appropriate method for the given task. There are also requirements that are partially contradictory and cannot be fulfilled in the same way:

- be as quick as possible, reliably detect the lack of continuity;
- it should be simple and can be done on site;
- preferably do not require special security measures;
- require minimal preparatory work;
- do not cause any changes in the condition of the workpiece;
- the equipment(s) should be simple and portable;
- the results can be permanently registered.

Aspects for choosing the test method:

- ability to reliably detect the desired discontinuity,
- the test site,
- size, shape, mobility of the product to be tested,
- size, design, surface fineness, accessibility of the area to be examined,
- the physical and chemical properties of the substance to be tested,
- requests related to the documentation (registry) of the examination,
- economy.

The CT examination is known as Computer Tomography, which is a branch of radiological diagnostics. The word tomography refers to slicing,

because in tomographic images, the subject of the examination can be seen divided into imaginary slices. Computed tomography is a further development of the traditional X-ray screening technique (Figure 7) [9].

CT machines therefore use X-ray radiation to create images, but the rays do not expose film, but detect them with the help of detectors, and then the reconstructed cross-sectional image is created from the electrical signals obtained from the detectors with the help of a computer. In the case of a tomographic scan, the examined object is illuminated with a thin, plane-like X-ray beam. The detector placed behind the object detects along a line where and how much of the beam has been absorbed.

With the beam, the body is illuminated from several directions in a given plane, and a drawing of the details located in the given plane (slice) unfolds from the measured intensity curves. The plane is then pushed away and rotated again. Once the procedure is completed, the spatial structure of the examined body can be mapped. By structure, we mean details that can be distinguished from the point of view of X-ray transmission, that is, the arrangement of material parts with different densities. Figure 8 summarizes the factors influencing the CT examination [10].

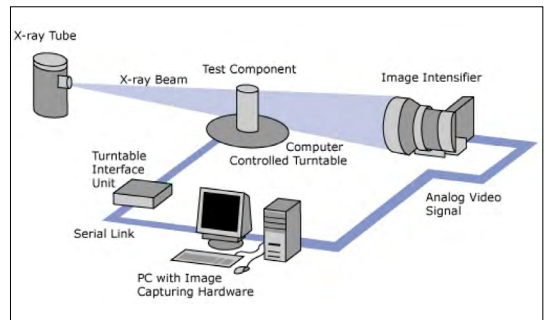


Figure 7. Computed tomography equipment scheme.

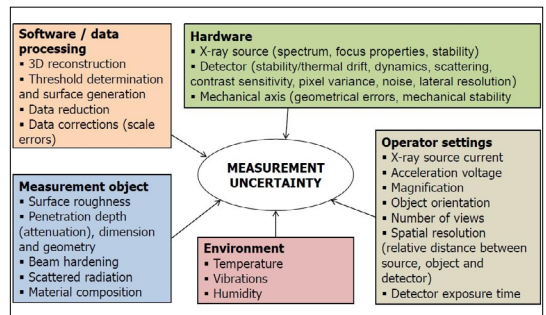


Figure 8. Factors affecting for CT examination.

4. Conclusions

The automotive industry is moving in a direction where it places great emphasis on reducing the weight of vehicles and thereby minimizing emissions. This weight reduction can be achieved mainly with new types of materials such as high-strength steels and aluminum alloys or cellular materials, including metal foams. Some of these non-destructive tests are essentially „quantitative”, i.e. they indicate that there is a given number of (one or more) discontinuities, but provide information on their „quality” (type) and spatial extent, or only with limited validity, while the other part of the tests is a procedure with both quantitative and qualitative results.

Acknowledgements

The author would like to thank the Hungarian State, the National Research, Development and Innovation Office and the European Union for the support of the project No. 2020-1.1.2-PIA-CI-KFI-2020-00081.

References

- [1] Ashby Michael F.: *Materials Selection in Mechanical Design*. Butterworth-Heinemann, Oxford, 2005.
- [2] García-Moreno F.: *Commercial Applications of Metal Foams: Their Properties and Production*. Materials, 9/2. (2016) 85. <https://doi.org/10.3390/ma9020085>
- [3] Sathurusinghe S. A. S. P., Herath K. R. B., Herath S. R.: *Elastic Properties of Open Cell Metallic Foams Using Finite Element Analysis and Homogenization Technique*. 45th IEP Convention 2012, 11.
- [4] Banhart J.: *Manufacturing Routes for Metallic Foams*. JOM, 52. (2000) 22–27. <https://doi.org/10.1007/s11837-000-0062-8>
- [5] Banhart J.: *Manufacture, Characterisation and Application of Cellular Metals and Metal Foams*. Progress in Materials Science, 46. (2001) 559–632. [https://doi.org/10.1016/S0079-6425\(00\)00002-5](https://doi.org/10.1016/S0079-6425(00)00002-5)
- [6] Kenesei P., Kádár Csi., Rajkovits Zs., Lendvai J.: *Fémhabok előállításának módszerei*. Anyagok Világa, 2/2. (2001).
- [7] Bagyinszki Gy.: *Anyagismeret és minősítés*. BMF Bánki Donát Gépészmérnöki Főiskolai Kar, Budapest, 2004.
- [8] Hareancz F., Kiss N.: *Alumíniumhabok ívhegesztésének vizsgálata*. Jelenkori Társadalmi és Gazdasági Folyamatok, 14/1. (2019) 61–69. <https://doi.org/10.14232/jtgf.2019.1.61-69>
- [9] Computed Tomography, Iowa State University, Center for Nondestructive Evaluation. <https://www.nde-ed.org/NDETechniques/Radiography/AdvancedTechniques/computedtomography.xhtml> (2022. 01. 17.)
- [10] Cantatore A., Müller P.: *Introduction to Computed Tomography*. Technical University of Denmark, Department of Mechanical Engineering, 2011 March.

Choosing the Adhesive for Microtensile Bond Strength Tests

Levente BORHY,^{1,a} Borbála LEVELES,^{2,b} Alexandra KEMÉNY^{1,c}

¹Department of Materials Science and Engineering, Faculty of Mechanical Engineering, Budapest University of Technology and Economics, Budapest, Hungary.

²Medicontur Medical Engineering Ltd., Zsámbék, Hungary.

^aborhy.levente@edu.bme.hu, ^bborbala.leveles@edu.bme.hu, ^ckemeny.alexandra@gpk.bme.hu

Abstract

Dental fillings are one of the most widespread minimal invasive procedures in modern restorative dentistry. Thanks to the advantages of recently developed filling materials, adhesive systems, and filling techniques, it is possible to create high strength, long-lasting dental fillings. Qualifying these structures is a complicated procedure; the most common method is the use of a microtensile bond strength test, for which specimens need to be formed and stabilised with adhesives in special jigs. During our research, three different cyanoacrylates were examined to find the ideal adhesive for bonding the metal and dentin and the metal and EverX short fibre composite, respectively.

Keywords: composite dental filling, microtensile bond strength test, adhesive systems.

1. Introduction

Materials science related to restorative dentistry and the methodology of teeth restoration is a dynamically developing field. Thanks to modern filling materials and filling techniques, high strength composite dental restorations can be created [1, 2].

With these newly developed materials, high-quality dental fillings can be created rapidly with a one-step bulk filling technique, compared to the traditional layering technique which is time-consuming. These composites and filling techniques are comparable by quantifying their properties to given stresses [2].

Therefore, it is necessary to examine the different types of filling techniques and materials, as the mechanical properties of finished dental restorations depend on several factors..

1.1. Structure of dental fillings

The composition of dentin, which extends from the crown to the root of the tooth and forms the main part, consists of approximately 70 % inorganic, 18 % organic material and 12% water. This tissue's composition and properties differ according to its location [3, 4].

The biomimetic approach is a novel, increasingly prominent field for restoring deep, Class I cavities (usually difficult to fill in one step), with mostly a short fibre reinforced composite as dentin replacement. A typical biomimetic restorative approach uses a combination of materials resembling the natural properties of the replaced tissues [5].

One of the most significant parameters in biomimetic restorations is the bond between the dentin and the dentin replacement composite. Improper adhesion can lead to filling detachment and secondary caries, the most common causes of failure in dental fillings [5, 6].

1.2. Test method

One of the most common methods for qualifying the bond between the dentin and the dentin replacement material is to perform microtensile bond strength tests. The conventional microtensile bond strength test is the most commonly used method [7, 8].

This measurement is suitable for examining small samples; therefore, several samples can be prepared from one tooth. Usually, prismatic specimens are used during the tests. Another widely

used type of specimen is dumbbell-shaped, in which the location of the failure can be determined in advance, but this is limited due to the rigid behaviour of the samples [4, 6].

In the latest studies, the microtensile bond strength test is used to qualify dental fillings [9–11]. Thus during this research, the method of sample binding was examined since the literature does not detail the exact steps.

Modern biomimetic dental fillings are of high strength, so the strength of the binding to the clamp must be greater than the adhesion between the dentin and the filler to test the dentin–filler connection properly. Our goal is to bond samples to clamps used in dental research with various commercially available cyanoacrylate adhesives and perform microtensile bond strength tests to determine which adhesives should be applied while binding the dentin or the composite to the metal clamp.

During our research, we performed tensile tests on previously removed wisdom teeth and on filling materials used in the daily practice of dentists.

2. Materials and methods

2.1. Materials

For the microtensile bond strength tests, three types of cyanoacrylate adhesives were used.

The first is Loctite Super Attak Power Easy (LSAPE) gel adhesive, which is easy to apply due to its high viscosity, and it is a high-strength adhesive.

The second is 3M Scotch-Weld Instant Adhesive PR100 (3M), a low-viscosity adhesive specifically for polymers that are difficult to bond.

Finally, we used Loctite Super Attak Brush On (LSABO) low-viscosity instant adhesive.

In all cases, the metal surface was cleaned with acetone and treated with a Toolcraft primer and polymerisation was accelerated with an activator at the end of the process.

The EverX Posterior short-fibre reinforced composite is used as filling material to replace the dentin in restorative dentistry. It has a low amount of polymerisation shrinkage so that it can create gap-free connections.

The teeth specimens were all cut from wisdom teeth removed for health reasons.

2.2. Preparation of specimens

From the removed wisdom teeth, prismatic specimens with a side length of ~1–1.5 mm and a height of ~8 mm were cut for microtensile bond

strength tests. First, the tooth's root was cut with a Buehler IsoMet 1000 diamond disc cutter, thus opening the pulp cavity, then it was filled up with Cosmedent Insure White Opaque dental composite. In the next step, slabs were cut perpendicular to the occlusal surface, and then 2-3 prismatic specimens were cut from each slab.

For the adhesion test of EverX composite, the composite was given form using a unique tool, cured with a polymerisation lamp, removed from the form and light-cured on several sides. In the next step, the sample was cut to the same size as the tooth sample.

2.3. Methods of measurements

In order to choose the adequate adhesive, tensile tests were performed on an Instron 5965 universal electromechanical material tester with a 5 kN load cell and a 1 mm/min crosshead speed.

During the examination, the specimens were bonded to generally used jigs with different adhesives.

Both the shear- and tensile stresses were calculated during the evaluation. In cases where sample failure occurred during the test, the material-specific tensile strength was obtained using the area of the beams' cross-section. In other cases, where the specimens slipped out of the bond, its cross-section lying on the clamp and the length of the binding were used to calculate shear strength, which qualifies the cyanoacrylate adhesives.

The aim of the measurement was to select an adhesive for the microtensile bond strength tests with which the adhesion to the test specimen can withstand a higher shear load than the tensile load of the specimen.

3. Results

Tensile tests were performed on the prepared prismatic specimens in the case of wisdom teeth and EverX. The tests were performed on 5-5 specimens with each cyanoacrylate in both cases. [Figure 1](#) shows the test results.

3.1. Examination of wisdom teeth

In addition to the quantitative results of the test, it should be noted that in the case of LSABO, one sample was fractured during the test, and in the case of 3M, each sample fractured before the adhesive had released.

3.2. Examination of EverX

It is also essential that the samples fixed with 3M adhesive were all fractured in the material; in

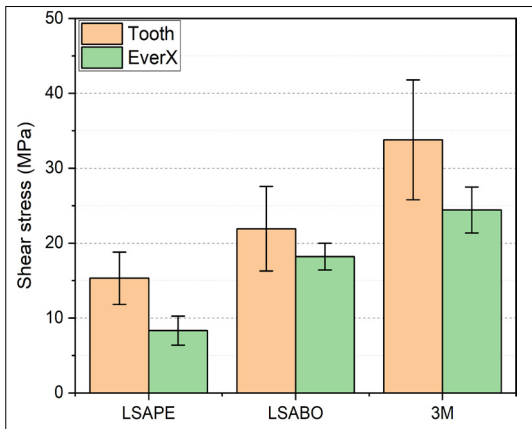


Figure 1. The shear strength of each examined adhesive

the case of LSABO, four samples were fractured, while with LSAPE, no sample failure occurred, except in the adhesive bond.

From the results obtained, it can be observed that all the tested adhesives form a greater bond strength with the tooth than with the EverX composite, but due to the uniqueness of teeth, these results have a higher deviation. In the case of the 3M and LSABO, the average shear bond strength is higher than the calculated value, as the samples fractured before the bond was released.

Due to the fracture of the samples, the tensile load capacity of the materials could be calculated. The average value of teeth specimens was 74 ± 16 MPa. in the case of EverX, it was 63 ± 6 MPa.

4. Conclusions

The test results provide an excellent base for comparing the adhesives examined in this study, both bonding to teeth and EverX. In both cases, it is clear that the values of the 3M adhesive far exceed the values of the bond strength of the other adhesives; furthermore, from the adhesives tested, this is the most suitable cyanoacrylate for performing microtensile bond strength tests for Class I dental restorations.

The results show that while every research group uses cyanoacrylate-based adhesives, the adhesive must be chosen carefully, even with the appropriate preparations.

Acknowledgements

The research reported above was approved by TUKEB under the license number of IV/8518-1/2021/EKU. The publication of the work reported herein has been supported by ETDB at BME.

References

- [1] Salim F. M.: *Tribological and mechanical characteristics of dental fillings nanocomposites*. Energy Procedia, 157. (2019) 512–521. <https://doi.org/10.1016/j.egypro.2018.11.215>
- [2] Ajaj R. A., Farsi N. J., Alzain L., Nuwaylati N., Ghurab R., Nassar H. M.: *Dental bulk-fill resin composites polymerization efficiency: A systematic review and meta-analysis*. Journal of Composite Science, 5/6. (2021) 149. <https://doi.org/10.3390/jcs5060149>
- [3] Giannini M., Soares C. J., De Carvalho R. M.: *Ultimate tensile strength of tooth structures*. Dental Materials, 20/4. (2004) 322–329. [https://doi.org/10.1016/S0109-5641\(03\)00110-6](https://doi.org/10.1016/S0109-5641(03)00110-6)
- [4] Hosoya Y., Kawada E., Ushigome T., Oda Y., Garcia-Godoy F.: *Micro-tensile bond strength of sound and caries-affected primary tooth dentin measured with original designed jig*. Journal of Biomedical Materials Research - Part B Applied Biomaterials, 77B/2. (2006) 241–248. <https://doi.org/10.1002/jbm.b.30433>
- [5] Garoushi S., Gargoum A., Vallittu PK., Lassila L.: *Short fiber-reinforced composite restorations: A review of the current literature*. Journal of Investigative and Clinical Dentistry, 9/3. (2018) e12330. <https://doi.org/10.1111/jicd.12330>
- [6] El Mourad A. M.: *Assessment of Bonding Effectiveness of Adhesive Materials to Tooth Structure using Bond Strength Test Methods: A Review of Literature*. The Open Dentistry Journal, 12. (2018) 664–678. <https://doi.org/10.2174/1745017901814010664>
- [7] De Munck J., Luehrs A. K., Poitevin A., Van Ende A., Van Meerbeek B.: *Fracture toughness versus micro-tensile bond strength testing of adhesive-dentin interfaces*. Dental Materials, 29/6. (2013) 635–644. <https://doi.org/10.1016/j.dental.2013.03.010>
- [8] Sano H., Chowdhury A., Saikaew P., Matsumoto M., Hoshika S. & Yamauti M.: *The microtensile bond strength test: Its historical background and application to bond testing*. The Japanese Dental Science Review, 56/1. (2020) 24–31. <https://doi.org/10.1016/j.jdsr.2019.10.001>
- [9] Alhenaki A. M., Attar E. A., Alshahrani A., Farooq I., Vohra F., Abduljabbar T.: *Dentin bond integrity of filled and unfilled resin adhesive enhanced with silica nanoparticles - an SEM, EDX, micro-Raman, FTIR and micro-tensile bond strength study*. Polymers (Basel), 13/7. (2021) 1093. <https://doi.org/10.3390/polym13071093>
- [10] Dao Luong M. N., Shimada Y., Turkistani A., Tagami J., Sumi Y., Sadr A.: *Fractography of interface after microtensile bond strength test using swept-source optical coherence tomography*. Dental Materials, 32/7. (2016) 862–869. <https://doi.org/10.1016/j.dental.2016.03.019>

- [11] Ahmed M. H., De Munck J., Van Landuyt K., Peumans M., Yoshihara K., Van Meerbeek B.: *Do universal adhesives benefit from an extra bonding layer?* Journal of Adhesive Dentistry, 21. (2019) 117–132.
<https://doi.org/10.3290/jjad.a42304>

Design of a High Performance Fiber-producing Machine

Hunor FÁBIÁN,¹ Attila GERGELY²

¹ University of Sapientia EMTE, Faculty of Technical and Human Sciences, Târgu Mureș, Advanced Mechatronics Systems profile, II. year, Târgu Mureș, Romania, fabianhunor2@gmail.com

² University of Sapientia EMTE, Faculty of Technical and Human Sciences, Târgu Mureș, Department of Mechanical engineering, Târgu Mureș, Romania, agergely@ms.sapientia.ro

Abstract

The aim of this work is to design a high-productivity, continuously operating fiber producing device utilizing the centrifugal force to yield polymeric nanofibers. The requirements for the design were 1) to provide a capillary-to-collector distance of 50-200 mm that could be adjusted automatically, 2) allow the rotational speed of the spinneret to be changed in the range of 0-25000 1/min and have continuous feeding. The equipment will form the basis of several research topics, such as the creation and study of solid dispersions of drugs, the development of pressure sensors, and the creation of porous filter membranes.

Keywords: *design, centrifugal spinning, nanofiber, control system.*

1. Introduction

Nanotechnology deals with material properties and functionality when the dimension of the produced item falls between 0.1 to 100 nm [1, 2]. Nanomaterials exhibit different properties than those of a bulk piece made of the same material. This is due to the nanometer scale dimensions and leads to some interesting properties with regards to the mechanical, thermal, optical, biological, magnetic and electronic behavior [3].

A good example of nanomaterial is fibers, that are used in several industries ranging from batteries, fuel cells, electric components, the air and space industry and drug carriers, to filters for gas and liquid applications. There are several techniques dealing with the production of nanofibers. Double component extrusion, phase separation, pattern synthesis, drawing, electrospinning and centrifugal spinning are a few that could be mentioned [4].

Electrospinning in particular is a well-studied polymeric nanofiber production technique that allows production of fibers below the micrometer range. The setup is simple and easy to use. Several polymers can be used to produce nanofibers with electrospinning. Electrospinning can be of two types: solution spinning or melt spinning. Solution spinning requires the use of a solvent

that solubilizes the polymer to yield a polymer solution. This method uses less energy; however the use of solvents could pose an environmental threat. Melt electrospinning utilizes heat to produce a polymer melt for the fiber production. Melt spinning produces fibers with larger diameters, in the couple of 10s of micrometer range and allows little control over the fiber diameter by the process parameters [5]. Electrospinning is a favourable method to produce nanofibers, however it has some disadvantages, such as the employment of a high electric field, the polymer solution or melt has to be electrically conductive and the production rate is very low, 0.01-0.5 g/h.

Centrifugal spinning to produce polymer-based nanofibers first appeared in the literature in the early 2010's. The technique uses centrifugal force to produce nanofiber instead of an electric field as in the case of electrospinning. During centrifugal spinning a head that contains the polymer solution and a few capillaries (Figure 3) spins at a high 1/min. Due to the arising centrifugal force a polymer solution jet exits on each capillary and travels from the rotating head to a stationary collector. During the process the solvent evaporates and the solidified polymer fiber deposit on the collector. Centrifugal spinning, even at laboratory scale, has a high production rate, 60 g/h/capillary [6].

2. Centrifugal Spinning Machine

2.1. Design Requirements

The designed centrifugal spinning machine has a similar design and the same working principle to the commercially available models. The objective was to produce a centrifugal spinning machine that could be used for both educational and research purposes at the Sapientia University, Faculty of Technical and Human Sciences – Târgu-Mureș. The design criteria were:

- the polymer solution feeding should be continuous (the majority of the centrifugal spinning machines reported in the literature work in a batch mode),
- the temperature and relative humidity could be measured,
- the speed of the spinning head could be controlled and the maximum speed should be approximately 30000 1/min,
- the capillaries could be changed
- the capillary-collector distance could be altered.

2.2. The Structure of the Centrifugal Spinning Machine

2.2.1. Frame

The frame is made of 30×30 mm Bosch Rexroth aluminum profiles, that are strong enough to withstand the arising mechanical stresses and on the other hand it allows a relatively easy assembly. The profile is anodized, thus it can withstand the potential corrosive nature of the utilized solvents. The frame has a 650×650×650 mm³ cube shape with a utilizable workspace of 650×650×430 mm³.

2.2.2. The 3-phase Electric Motor

An APS 6374 brushless DC (BLDC) electric motor was selected to rotate the spinning head (Figure 2). The motor provides a maximum of 3200 W power and a maximum 1/min of 38400. The BLDC motor could be supplied by a maximum of 48 V and the rotation speed control is carried out with an appropriate phase control unit.

2.2.3. The BLDC Motor Controller

The brushless DC electric motors, also known as electric commutation direct current motors (ECDC) are servo motors with a DC feed that has an electrically controlled commutating system. For such electric motors, the current used is directly proportional to the torque, while the voltage is proportional to the speed.

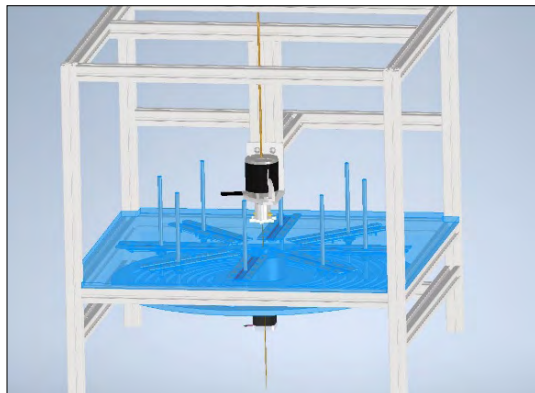


Figure 1. The 3D image of the designed centrifugal spinning machine.



Figure 2. The APS 6374 BLDC electric motor.

In a BLDC motor the coils (electromagnets) do not move, instead the permanent magnets rotate, and the armature is stationary. The brush-commutator system is replaced with an electric control unit.

2.2.4. The Rotating Head

The rotating head, responsible for the fiber production, is attached to the shaft of the BLDC motor. The continuous feed is accomplished by a syringe pump, that is connected to the rotating head by a copper pipe. A 5 mm diameter hole is drilled in the shaft of the motor along its axis to allow the copper pipe to reach the rotating head, thus allowing the polymer solution to reach the capillaries. The rotating head is designed as an assembly of two pieces to allow for easy cleaning and assembly. The upper piece, 1 in Figure 3, connects

to the shaft by a tight tolerance and further secured by two screws. The lower part, 2 in **Figure 3**, of the rotating head screws on to the first one.

2.2.5. The Collector

The fibers deposit on the collector, thus vertical rods are placed along a circle, the diameter of which can be altered, as illustrated in **Figure 5**. The working principle of the mechanism that allows the change of the circle's diameter, thus the movement of the collector rods, is similar to that of a lathe chuck. Eight stainless steel rods form the collector placed along a circle with axis parallel to the rotating head. There are two major units to the mechanism: a stationary unit that guides the collector rods, thus the radial movement is possible, and a moving, rotating unit, that contains eight Archimedes spiral shaped channels. The equation of the Archimedes' spiral and the rotating angle of the rotating unit allows the calculation of the exact positions of the collector rods with respect to the rotating head.

2.2.6. The Drivetrain of the Collector

A stepper motor equipped with a speed reducer, 1 in **Figure 5**, is responsible for the rotating movement of the collector. The speed reducer has a gear ratio of $i = 50$. The motor drives the moving unit of the collector via a toothed belt with a reduction ratio of $i = 14$, 2 in **Figure 5**, thus providing the required torque.

2.2.7. The Driver of the Stepper Motor

The stepper motor is controlled by a digital DM332T driver. This driver has been chosen due to its dependability and ease of programming. The bipolar stepper motor can be controlled by connecting it to the right connections of the driver. The "PUL" connection is responsible for the number of steps the motor has to take, the "DIR" connection provides the direction of the rotation, and the motor is powered by the "ENA" connection with 5V.

2.2.8. The Central Control Unit

The centrifugal spinning machine will be controlled by a PLC unit, that allows the adjustment of the rotating speed and capillary-collector distance. The PLC unit grants the industrial reliability and flexible programming of the centrifugal spinning machine, that must operate in a continuous fashion. A Siemens Sematic S7-300CPU PLC unit has been chosen for this purpose.

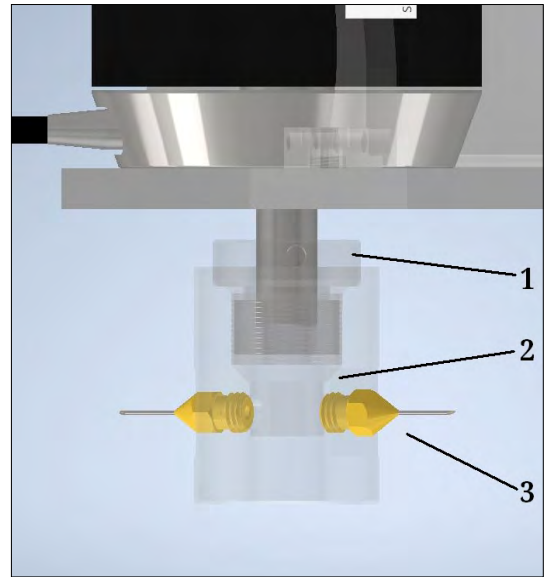


Figure 3. 3D model of the rotating head with the capillaries attached: 1 – upper part, 2 – lower part, 3 – attached capillaries.

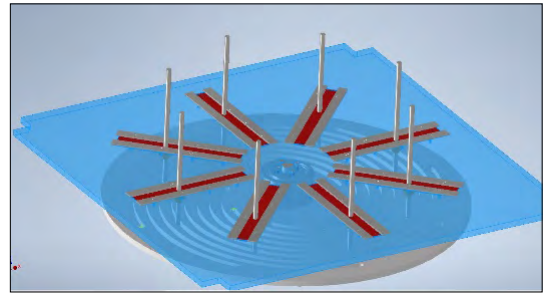


Figure 4. Circular placement of the collector rods.

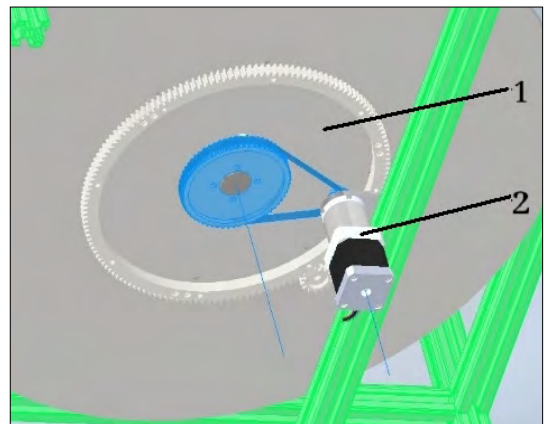


Figure 5. The drivetrain of the collector: 1 – stepper motor and 2 – toothed belt drive.

4. Conclusions

In conclusion, the presented design steps result in a continuously operated, automated centrifugal spinning machine that follows the cost-effective design principles.

References

- [1] Nalwa H. S.: *Handbook of nanostructured materials and nanotechnology*. Academic press, San Diego 2000.
- [2] Ko F. K., Wan, Y.: *Introduction to Nanofiber Materials*. Cambridge University Press, United Kingdom, Cambridge 2014.
- [3] Laurencin C. T., Nair L. S.: *Polyphosphazene Nanofibers for Biomedical Applications: Preliminary studies*. NATO Science Series II, Mathematics, Physics and Chemistry, 169. (2004) 283–302. <https://doi.org/10.1007/978-1-4020-2550-1>
- [4] Alghoraibi I., Alomari, S.: *Different methods for nanofiber design and fabrication*. In Handbook of nanofibers (eds.: Barhoum A., Bechelany M., Makhlof A.), Springer International Publishing, 2018. 1–46. https://doi.org/10.1007/978-3-319-42789-8_11-2
- [5] Brown T. D., Dalton P. D., Hutmacher D. W.: *Melt electrospinning today: An opportune time for an emerging polymer process*. Progress in Polymer Science, 56. (2016) 116–166. <https://doi.org/10.1016/j.progpolymsci.2016.01.001>
- [6] Ren L., Ozisik R., Kotha S. P.: *Rapid and efficient fabrication of multilevel structured silica micro/nanofibers by centrifugal jet spinning*. Journal of Colloid and Interface Science, 425. (2014) 136–142. <https://doi.org/10.1016/j.jcis.2014.03.039>

Wear Modelling of Total Knee Replacements

Gusztáv FEKETE,¹ Singh TEJ,² Endre JÁNOSI³

Eötvös Loránd University, Faculty of Informatics, Savaria Institute of Technology, Szombathely, Hungary

¹fg@inf.elte.hu ²sht@inf.elte.hu ³je@inf.elte.hu

Abstract

Beside prosthesis loosening, wear is the mechanical factor that most significantly influences the lifetime of total knee replacements (TKRs), which can only be described by a number of interrelated parameters. The examination of the wear occurring in TKRs is mostly carried out as a combination of experiments and mathematical modeling. The experiment can provide the real magnitude of wear, while the model is intended to mathematically describe the relationship between wear and the wear-inducing parameters. On the one hand, this study focuses on the mathematical description of wear as a natural-technical phenomenon, presenting the most important analytical and numerical models, while also providing an open view on exciting questions that still await answers.

Keywords: *wear, knee joint, prosthesis, Archard wear model.*

1. Introduction

Despite the fact that researchers and prosthesis manufacturing companies work together to create more reliable and efficient implants, there are still numerous cases of TKR failure. The main reasons why TKR failures still occur are infection of the knee joint, loosening of the TKRs, and the impermissible amount of wear in the implants. Wear can develop in the knee joint (or any other joints) for several reasons. It may be due to the incongruence of the joint itself, or due to the natural instability of the joint.

It must be noted that wear is a phenomenon that can be described only by multiple interrelated parameters, which must be treated as a system and not as a material property [1].

Its importance should be highlighted, since this mechanical factor has the most significant effect on TKR lifetime [2, 3], while its influence strongly depends on the local kinematics taking place in the knee joint [4, 5].

Wear is directly and indirectly influenced by several parameters. The most important direct parameters are the sliding length, the load and the relative wear factor.

The most effective way to examine wear is a combination of experiments and mathematical

models. It is important to mention, with regard to the experiments, that several important parameters, which are included in the measurements as adjustable parameters, unfortunately do not appear in mathematical models.

An example is the slide-roll ratio (S/R), which is a value that varies between 0 and 1. If the value is 0, the two surfaces purely roll on each other, while if it is 1, they predominantly slide. Between the two, sliding and rolling appear together.

The magnitude of this factor is usually applied between 0 and 40% during tribological tests e.g. on pin-on-disc, ball-on-disc or on knee simulators [6, 7]. These values are based on as the results of previous theoretical models [8, 9].

These results are applicable for connections with simple geometry, such as pin-on-disc and ball-on-disc type tests, since a smooth flat surface (pin) or a spherical surface (ball) slides and rolls on the surface of a disc, therefore the condition of constant slide-roll provides a suitable kinematic description.

However, this condition is no longer adequate if the geometry is complex. The latest results related to this topic show that the constant slide-roll ratio cannot be applied to TKRs [10, 11], since the complex geometry creates extremely complex local movements.

Another particularly important parameter, which should definitely be highlighted, is the so-called cross-shear ratio (CSR). This parameter appeared in the application of ultra-high molecular weight polyethylene (UHMWPE) in TKRs, as it has a special „motion-dependent” property. In case of TKRs, the tibial part is made of UHMWPE, while the femoral part is made of stainless steel. When the femoral and tibial parts come into contact with each other, as a result of sliding, the orientation of the polyethylene molecules changes and it is arranged in the direction of sliding. This type of arrangement of the molecules causes surface hardening, which increases the wear resistance of the material in this particular direction.

However, while the wear resistance of the material increases in one direction, it strongly decreases in the direction perpendicular to it. This ratio is expressed by cross-shear ratio, which in the literature is often related to the relative wear factor [12].

The purpose of this article is to provide insight into the mathematical modeling of TKR wear. The article provides an overview of the most frequently used models in the literature, as well as a description of the creation of a model that is already in use..

2. Models

Most authors start their modeling by the use of a commonly applied wear model. This is the so-called Archard model [13].

$$dW = k \cdot F_N \cdot ds, \quad (1)$$

where k is the so-called specific wear factor (mm^3/Nm), which is a constant depending on the material property, F_N is the force occurring between the pressed surfaces, and ds is the instantaneous sliding length.

Despite its simplicity, the Archard model is still widely used in the relevant literature as a starting model.

Of course, in this form, it can only give a distant estimate, which is why the authors augment the model with additional parameters, such as the previously mentioned cross-shear factor, slide-roll ratio or the friction coefficient. It should be noted that there are some authors who do not define concentrated force (F) as load in their model, but surface pressure (p).

In **Table 1** we have summarized the most often used wear models, which were used in the connection of TKRs.

Table 1. Wear models

Modell	p/F	s	CSR	S/R	μ
Archard [13]	P	o	x	x	x
Hussin [14]	P	o	x	x	x
Innocenti [15]	P	o	x	x	o
Turell [16]	p	o	o	x	o
O'Brien [17]	p	o	o	x	o
Abdelgaied [18]	F	o	o	x	o
Fekete [19]	F	o	x	o	o

As we see in the table, the majority of authors have not considered all parameters (x). In the best cases, three main parameters were added to their model, compared to the original Archard equation. In the next section, we present a way to expand and further develop this basic model.

3. Modelling steps

3.1. Analytical modeling

The first step is to consider the slide-roll ratio in the wear equation. The instantaneous slide length can also be written as the product of slip velocity and time.

$$ds = v_{slide}(t) \cdot dt \quad (2)$$

Based on our previous study [20] if we interpret slide-roll ratio as instantaneous velocities instead of instantaneous arc lengths, we can also use it according to the following relationship:

$$S/R(t) = \frac{v_{CTt}(t) - v_{CFt}(t)}{v_{CTt}(t)}, \quad (3)$$

where v_{CTt} and v_{CFt} are the tangential velocities interpreted at the contact point for the tibia and femur respectively. The difference between these velocities gives the slip velocity ($v_{CTt} - v_{CFt} = v_{slide}$). Setting this expression for the slip velocity and substituting back into equation (1):

$$dW = k \cdot F_N \cdot v_{CTt} \cdot S/R(t) \cdot dt, \quad (4)$$

we obtain the augmented Archard equation, in which the slide-roll ratio is also taken into account.

Now consider the effect of the friction coefficient as follows: The wear mechanism between the femoral and tibial surfaces is assumed to be abrasive, which means that during contact, the harder metal femoral part ploughs into the softer polyethylene surface (**Figure 1**).

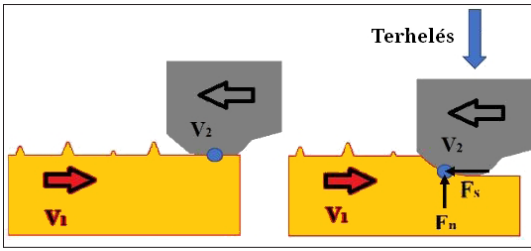


Figure 1. Description of abrasive wear mechanism.

In the abrasive wear mechanism, the frictional component is responsible for creating such a shear stress in the upper surface of the material that it begins losing small debris. Therefore, it provides us a more precise approximation if the friction force is introduced into our wear equation:

$$F_s = \mu_k \cdot F_N, \tag{5}$$

If we substitute this expression into equation (4), we obtain the following relation:

$$dW = k \cdot \mu_k \cdot F_N \cdot v_{CTt} \cdot S/R(t) \cdot dt \tag{6}$$

In this way, we have created a model, which involves the factors with the most significant influence on wear, except cross-shear ratio. As a next modeling step in the future, we shall integrate this missing factor into our model.

3.1. Numerical modeling

To be able to determine the evolution of wear on both sides of a TKR (lateral and medial), it is necessary to take the geometry into account. This is a challenging task to deal with analytically, since the function of the compressive force in the connection of the femoral and tibial parts of the TKR must be determined during the movement.

Due to this problem, it is advisable to create a multibody dynamic (MBD) system and determine the forces in question using an adequate software. This can be performed in the following steps (Figure 2).

The first step is to select the wear model, which in this case will be equation (6). This is a linear first-order ordinary differential equation. To solve the equation, i.e. to calculate the wear volume, we need the compression force determined from the MBD simulations on the lateral and medial sides of the tibial plate. For the simulations, we used three different prosthesis geometries. The aim was to determine the amount of wear in the tibial part of the TKRs, and to classify which TKR has a higher chance of failure (Figure 3).

Using the TKR geometries, we created the MBD

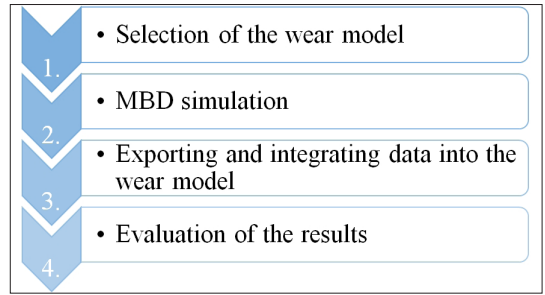


Figure 2. Algorithm of the numerical solution.

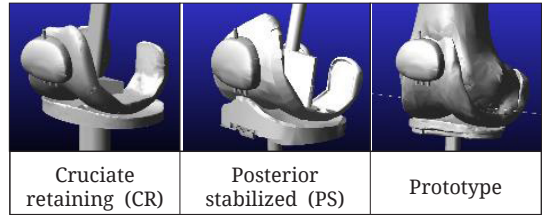


Figure 3. The applied TKRs

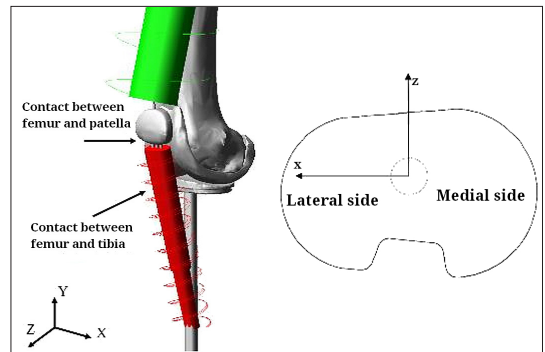


Figure 4. The applied MBD model.

models in MSC.ADAMS (Figure 4).

The boundary conditions were applied identically to all models.

After starting the simulation, the lateral and medial sides of the tibial part are in contact with the surfaces of the femoral part. MSC.ADAMS simultaneously stores contact points and forces for later evaluation. The resulting position vectors allow the differentiation of the lateral and medial sides, as well as the location of the contact forces on the surfaces. These force functions, as a function of time, serve as input to equation (6), which can be calculated as follows:

$$dW_{lat} = k \cdot \mu_k \cdot F_{cn,lat}(t) \cdot v_{CTt}(t) \cdot S/R(t) \cdot dt \tag{7}$$

$$dW_{med} = k \cdot \mu_k \cdot F_{cn,med}(t) \cdot v_{CTt}(t) \cdot S/R(t) \cdot dt, \tag{8}$$

where $F_{cn.med}$ and $F_{cn.lat}$ are the forces obtained from the simulations. After creating the wear functions, time as a variable was replaced by the knee flexion angle (α).

4. Results

To evaluate the results, we introduced parameters that not only quantify the wear, but also provide deeper insight into the physiological effect of wear on the TKRs. In addition to the lateral and medial side wear, we introduced a new quantity, the so-called amount of total wear:

$$TW(\alpha) = (W_{med.}(\alpha) + W_{lat.}(\alpha)) \tag{9}$$

Furthermore, the magnitude of the relative lateral and medial wear:

$$RW_{lat.}(\alpha) = \frac{W_{lat.}(\alpha)}{TW(\alpha)} \cdot 100 \tag{10}$$

$$RW_{med.}(\alpha) = \frac{W_{med.}(\alpha)}{TW(\alpha)} \cdot 100 \tag{11}$$

These quantities can be used to express the so-called wear imbalance:

$$WIB(\alpha) = RW_{medial}(\alpha) - RW_{lateral}(\alpha) \tag{12}$$

Wear imbalance demonstrates, as a percentage, how much medial wear deviates compared to lateral wear. It also implies that if a TKR is exposed to uneven medial load (and wear) then a so-called

hollowing mechanism can commence on the above-mentioned TKR plateau. In the long term, hollowing leads to the point that the physiological tibiofemoral alignment of the TKR will be tilted and this abnormal tilt becomes a wear-inducing factor [21].

Let us review the results after the introduced wear factors. First, we determined the amount of total wear for all prostheses (Figure 5):

Then, we determined the amount of lateral and medial wear for each TKR separately (Figures 6, 7 and 8).

Last but not least, by using these results, we created the most important result: the wear imbalance function (Figure 9):

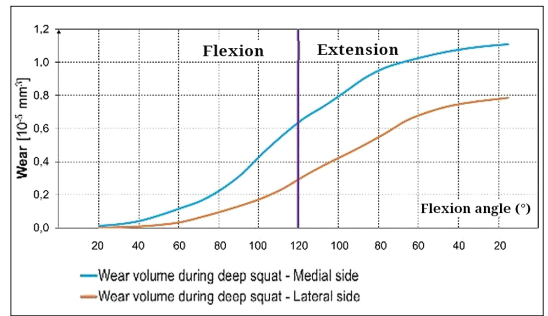


Figure 7. Lateral and medial wear (CR).

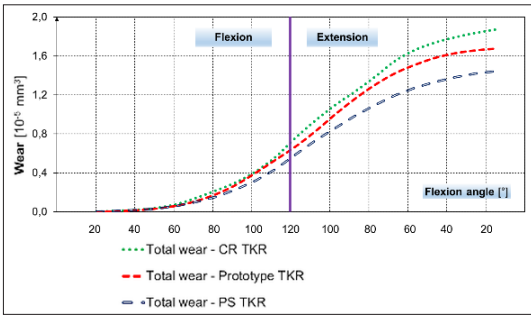


Figure 5. Total wear in different TKRs.

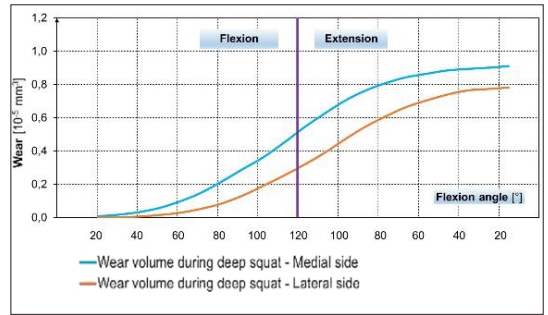


Figure 8. Lateral and medial wear (Prototype).

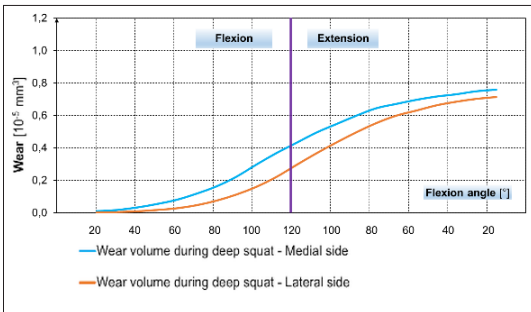


Figure 6. Lateral and medial wear (PS).

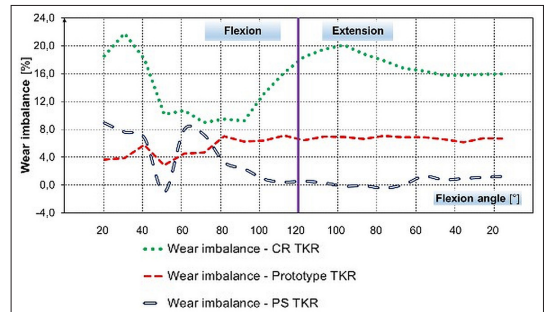


Figure 9. Wear imbalance function of different TKRs.

4. Conclusions

The wear results clearly highlight that the Bio-tech PS TKR (Figure 6) provided the lowest total wear with the least wear imbalance (approximately 2.3% averaged WIM). Such wear propagation on both sides of the tray can ensure that the „worn-through” stage would be postponed and implant revision could be significantly prolonged.

As we look at the following result (Figure 7), the CR type prosthesis performed ~23% higher total wear compared to the PS type. Even less favorably, the averaged lateral and medial wear imbalance was ~15.6%, which can lead to severe abrasion on the medial side and possible TKR retrieval before time.

A prototype TKR (Figure 8), designed by the late Professor Gábor Krakovits, has also been included in the investigations, which yielded the following results: this specific TKR produced only 13.7% more wear compared to the reference PS TKR while the averaged wear imbalance between the lateral and medial side was only 5.9%.

To have an adequately balanced wear on both sides, it would be required that the percentage difference should not exceed 5%, which is a generally accepted level in engineering. As can be seen, only the PS could stay within such limits, while the Prototype TKR was close to it.

Therefore, the CR type TKR should be modified in its geometry in order to avoid generating high wear imbalance on its medial side, or even TKR failure.

Acknowledgment

The study was supported by National Research, Development and Innovation Fund under the ÚNKP-21-5 New National Excellence Program of the Ministry of Innovation and Technology and the János Bolyai Research Grant of the Hungarian Academy of Sciences (BO/00047/21/6).

References

- [1] Karlhuber M.: *Development of a method for the analysis of the wear of retrieved polyethylene components of total knee arthroplasty*. Thesis, Technical University of Hamburg, Germany, 1995.
- [2] Kurtz S. M.: *UHMWPE Biomaterials handbook*. San Diego: Elsevier; 2009.
- [3] O'Brien S., Luo Y., Wu C., Petrak M., Bohm E., Brandt J. M.: *Computational development of polyethylene wear model for the articular backside surfaces in modular total knee replacements*. Tribology International, 59. (2013). 284–91. <https://doi.org/10.1016/j.triboint.2012.03.020>
- [4] Wimmer M. A., Andriacchi T. P.: *Tractive forces during rolling motion of the knee: Implications for wear in total knee replacement*. Journal of Biomechanics, 30. (1997) 131–137. [https://doi.org/10.1016/s0021-9290\(96\)00112-1](https://doi.org/10.1016/s0021-9290(96)00112-1)
- [5] Wimmer M. A., Andriacchi T. P., Natarajan R. N., Loos J., Karlhuber M., Petermann J., Schneider E., Rosenberg A. G.: *A striated pattern of wear in ultrahigh-molecular-weight polyethylene components of Miller-Galante total knee arthroplasty*. The Journal of Arthroplasty, 13. (1998) 8–16. [https://doi.org/10.1016/s0883-5403\(98\)90069-9](https://doi.org/10.1016/s0883-5403(98)90069-9)
- [6] Patten E. W., Van Citters D., Ries M. D., Pruitt L. A.: *Wear of UHMWPE from sliding, rolling, and rotation in a multidirectional tribo-system*. Wear, 304. (2013) 60–66. <https://doi.org/10.1016/j.wear.2013.04.017>
- [7] Patten E. W., Van Citters D., Ries M. D., Pruitt L. A.: *Quantifying cross-shear under translation, rolling, and rotation, and its effect on UHMWPE wear*. Wear, 313. (2014) 125–134. <https://doi.org/10.1016/j.wear.2014.03.001>
- [8] McGloughlin T., Kavanagh A.: *The influence of slip ratios in contemporary TKR on the wear of ultra-high molecular weight polyethylene (UHMWPE): An experimental view*. Journal of Biomechanics, 31. (1998) 8. [https://doi.org/10.1016/s0021-9290\(98\)80015-8](https://doi.org/10.1016/s0021-9290(98)80015-8)
- [9] Hollman J. H., Deusinger R. H., Van Dillen L. R., Matava M. J.: *Knee joint movements in subjects without knee pathology and subjects with injured anterior cruciate ligaments*. Physical Therapy, 82. (2002) 960–972. <https://doi.org/10.1093/ptj/82.10.960>
- [10] Nägerl H., Frosch K. H., Wachowski M. M., Dumont C., Abicht Ch., Adam P., Kubein-Meesenburg D.: *A novel total knee replacement by rolling articulating surfaces. In vivo functional measurements and tests*. Acta of Bioengineering and Biomechanics, 10. (2008) 55–60.
- [11] Fekete G., Csizmadia B. M., Wahab M. A., De Baets P., Vanegas-Useche L. V., Bíró I.: *Patellofemoral model of the knee joint under non-standard squatting*. Dyna Colombia, 81. (2014) 60–67. <https://doi.org/10.15446/dyna.v81n183.36171>.
- [12] Mattei L., Di Puccio F., Ciulli E.: *A comparative study of wear laws for soft-on-hard hip implants using a mathematical wear model*. Tribology International, 63. (2013) 66–77. <https://doi.org/10.1016/j.triboint.2012.03.002>
- [13] Archard J. F., Hirst W.: *The wear of metals under unlubricated conditions*. Proceedings of the Royal Society, A 236. (1956) 397–410. <https://doi.org/10.1098/rspa.1956.0144>
- [14] Hussin M. S., Fernandez J., Ramezani M., Kumar P., Kelly P. A.: *Analytical and computational sliding wear prediction in a novel knee implant: a case study*. Computer Methods in Biomechanics and Biomedical Engineering, 23/4. (2020) 1–13.

- <https://doi.org/10.1080/10255842.2019.1709118>
- [15] Innocenti B., Labey L., Kamali A., Pascale W., Pianigian S.: *Development and Validation of a Wear Model to Predict Polyethylene Wear in a Total Knee Arthroplasty: A Finite Element Analysis*. Lubricants, 2/4. (2014) 1–13.
<https://doi.org/10.3390/lubricants2040193>
- [16] Turell M, Wang A, Bellare A.: *Quantification of the effect of cross-path motion on the wear rate of ultra-high molecular weight polyethylene*. Wear, 255. (2003) 1034–1039.
[https://doi.org/10.1016/S0043-1648\(03\)00357-0](https://doi.org/10.1016/S0043-1648(03)00357-0)
- [17] O'Brien S. T., Bohm E. R., Petrak M. J., Wyss U. P., Brandt J-M.: *An energy dissipation and cross shear time dependent computational wear model for the analysis of polyethylene wear in total knee replacements*. Journal of Biomechanics, 47. (2014) 1127–1133.
<https://doi.org/10.1016/j.jbiomech.2013.12.017>
- [18] Abdelgaied A., Liu F., Brockett C., Jennings L., Fisher J., Jin Z.: *Computational wear prediction of artificial knee joints based on a new wear law and formulation*. Journal of Biomechanics, 44. (2011) 1108–1116.
<https://doi.org/10.1016/j.jbiomech.2011.01.027>
- [19] Fekete G.: *Computational study on lateral and medial wear characterization in knee implants by a multibody dynamic system*. Acta Mechanica, 232. (2021) 1075–1086.
<https://doi.org/10.1007/s00707-020-02868-4>
- [20] Fekete G., De Baets P., Wahab M. A., Csizmadia B. M., Katona G., Vanegas-Useche L. V., Solanilla J. A.: *Sliding-rolling ratio during deep squat with regard to different knee prostheses*. Acta Polytechnica Hungarica, 9. (2012) 5–24.
- [21] Wasielewski R. C., Galante J. O., Leighty R. M., Natarajan R. N., Rosenberg A. G.: *Wear patterns on retrieved polyethylene tibial inserts and their relationship to technical considerations during total knee arthroplasty*. Clinical Orthopaedics and Related Research, 299. (1994) 31–43.

Analysis of Fibre Laser’s Optical Construction from the End of the Beam Guiding Optical Fibre to the Focal Spot

György MESZLÉNYI,¹ Enikő BITAY²

¹ Obuda University, Bánki Donát Faculty of Mechanical and Safety Engineering Faculty, Budapest, Hungary, meszlenyi.gyorgy@uni-obuda.hu

² University of Sapientia, Faculty of Technical and Human Sciences, Târgu Mureş, Department of Mechanical engineering, Târgu Mureş, Romania, ebitay@ms.sapientia.ro

Abstract

In material-processing fiber lasers, the resonator in the closed box produces the laser radiation. Even with the same resonator, the diameter of the laser beam transporting fiber optics and the properties of the optical elements in the laser focusing head decide the cross-section of the focused laser beam used for machining. If we summarize the formulas in different sources in the literature, we can predict the effect of each optical element: what will happen if we choose another focusing lens, put a beam expander in the system, set on the beam expander how many times the laser beam expands. The other important point is that if we want to repeat an experiment or start a production process based on a scientific publication, then in addition to the resonator, it would be good to know the data of the optical elements in the focusing head, which is usually incomplete in the presented articles, but we can determine them approximately using the four formulas listed in the article.

Keywords: *fibre laser, laser micromachining, focusing head.*

1. Introduction

Laser radiation of fibre lasers in material processing is generated by a resonator in a closed box, where laser diodes convey their energy to the excited optic fibre equipped with a Bragg grating, functioning as the reflective and the partially transmissive end mirrors of the resonator. From here, the laser delivery fibre optics transmit radiation to the focusing head. In our present article we have analysed fibre lasers used in micro-machining.

In the focusing head the laser radiation exits the laser delivery fibre optics within a given bevel angle, characterised by the numerical aperture of the optical fibre. The radiation exiting the laser delivery fibre optics is collimated by the collimator lens, followed by an optional beam expander. Then the focusing lens focuses the laser beam onto the work-piece, The relative movement of the beam to the workpiece executes the planned operation, which may be drilling, cutting, welding etc. The quantities, symbols and units of measure used in the article are shown in **Table 1** using the

regular units of measurement for micro-machining, although wavelength is usually given in nanometers, and formulae (1) and (2) only provide results in micrometres if the wavelength is also given in micrometres.

In laser machining, the laser, i.e. focal spot diameter, the cross-sectional characteristic of the focused beam plays an important role, as the focused beam is the non-contact tool that performs machining through conveyance of energy. The formulae for the diameter of the focal spot are identical in several literature sources, but to achieve a common format, the radius must be doubled at times to obtain the diameter and the beam quality parameters must also be converted by entering the reciprocal value of the K beam propagation factor, i.e. M^2 beam quality factor into the formula (1) [1, 2].

$$d_{f0} = \frac{4\lambda M^2 f}{B_e d_b \pi} \quad (1)$$

Here λ is the wavelength of laser radiation, f is the focal length of the lens focusing the laser

beam onto the workpiece, M^2 is the beam quality factor, indicating how many times the diameter of the focal spot of the beam examined is bigger in comparison to the ideal Gaussian beam, d_b is the diameter of the close collimated laser beam before the focusing lens. If the close collimated laser beam incident on the focusing lens is expanded, the d_b beam diameter below is multiplied by the dimensionless beam expansion number (B_e), indicating the factor by which the beam diameter has been increased in comparison to the unexpanded diameter [1]. It follows from the formula for the spot diameter of the focused laser beam (1) that the smaller the value of the M^2 factor is, the smaller area the energy of the laser can be concentrated on.

The Rayleigh length is the length measured from the focal plane in the direction of beam spread, at which the area of the laser spot is doubled and the beam radius is increased by a factor of square root two, therefore the impulse energy per unit of surface area is halved in comparison to what it can be calculated in the focal spot. Generally, the beam is considered to be in focus within the double of the Rayleigh length. Its formula is very similar to that of the laser spot diameter, except that the focal length of focusing lens and the beam diameter before the lens are squared here (2) [1].

$$Z_R = \frac{4\lambda M^2 f^2}{B_e^2 d_b^2 \pi} \tag{2}$$

What further justifies this analysis is that the part of the laser beam used for laser machining is near the focal spot, and it is interesting to

Table 1. Symbols, descriptions and units of measure of the quantities used in the article

Symbols	Descriptions	Units of measure
f	the focal length of the lens focusing the laser beam onto the workpiece	mm
f_{coll}	the focal length of collimator collimating the laser beam	mm
d_{fc}	the core diameter of the optical fibre delivering the laser beam	μm
d_b	the diameter of the close collimated laser beam before the focusing lens	mm
d_{f0}	the focal spot diameter	μm
λ	wavelength of laser radiation	μm
M^2	the beam quality factor	
Z_R	Rayleigh length	μm

know where the focal spot is, what the diameter of the focal spot is and the double Rayleigh length within which it is possible to work with the laser. What further advantages does examination of the two quantities above have? Based on these two variables, the geometry of the focused beam can be described using functions: the beam diameter as a function of the z coordinate in the direction of beam propagation, with z_0 being the z coordinate of the focal plane: [1].

In the literature another formula can also be found for determining the focal spot diameter of fibre lasers, in which f is the focal length of the lens focusing the laser beam onto the workpiece, d_{fc} is the core diameter of the optical fibre delivering the laser beam, and f_{coll} is the focal length of collimator collimating the laser beam (3) [3, 4]. This formula is referred by both sources of literature as approximative, so the figures obtained with their help are given to two significant figures. In another article the formula is extended by a beam expander multiplication factor, i.e. a dimensionless number (B_e) (4) [5].

$$d_{f0} = \frac{d_{fc} f}{f_{coll}} \tag{3}$$

$$d_{f0} = \frac{d_{fc} f}{f_{coll} B_e} \tag{4}$$

2. Analysis

The optical elements discussed so far and the beam path of the laser head are shown in Figure 1 with the laser head shown in Figure 2, where the laser delivery fibre optics can be seen with the yellow protective cover, as well as the focusing head with a 45 degree angle mirror, diverting the beam in the vertical direction by 90 degrees.

Even in case of identical resonators, it is the diameter of the laser delivery fibre optics and the properties of the optical elements in the focusing head that determine the cross-section of focused beam used for machining. If we summarize the formulae (1), (2), (3) and (4) found in the related literature and other sources, the effect of the particular optical elements can be predicted: e.g. what happens if another focusing lens is chosen, a beam expander is inserted into the system, or if the adjustment of this latter is modified. These changes may be necessary if the machining tasks change significantly: if a material of significantly different absorption factor, material thickness or a workpiece with different shape may have to be machined at unaltered wavelength of the laser radiation. Replacement of the focusing lens

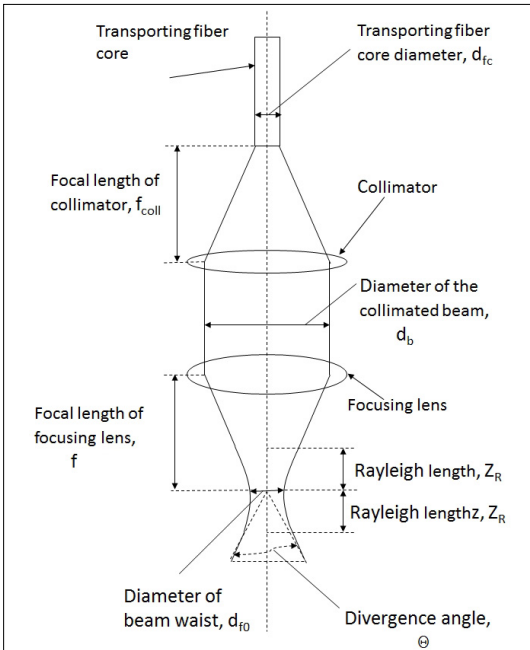


Figure 1. Visualization of the properties of focused laser beams discussed so far.

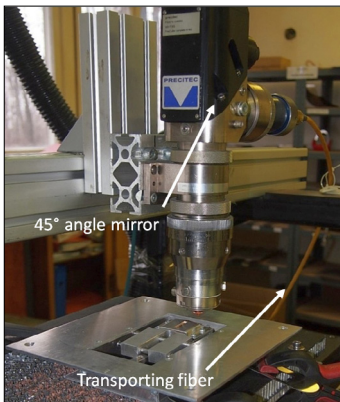


Figure 2. The focusing head for the laser equipment.

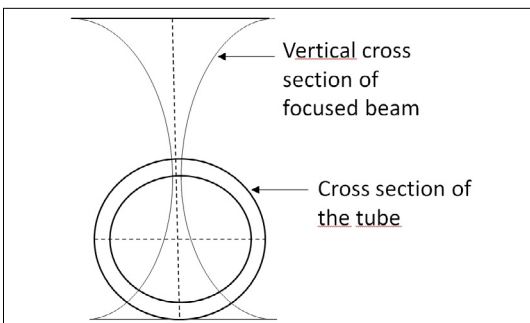


Figure 3. Longitudinal section of focused laser beam upon cutting a pipe.

or the integration of the beam expander system can be carried out in an experimental laser arrangement, but in case of a system provided by a particular supplier such conversions must be ordered from the manufacturer, also taking into account the aspects of laser safety.

The other important aspect is if we wish to repeat an experiment or launch a production process based on a scientific publication, then it would help to know the specifications of the optical elements in the focusing head, which are usually not communicated fully in the article introduced, but which can be approximated with the help of the four formulae listed above. Articles introducing laser machining usually fail to provide the curvatures and refractive indexes of the lenses in the focusing head, therefore the beam delivery software used in the optical design cannot perform calculations due to missing input data.

Analysing formula (1), if the focal length of the focusing lens is reduced, then theoretically the spot size also decreases linearly, and it follows from formula (2) that the Rayleigh length decreases quadratically. Analysing formula (1), if expanding the laser beam by a factor of x , then theoretically the spot size decreases according to the $1/x$ function, and it follows from formula (2) that the Rayleigh length decreases according to the $1/x^2$ function. The ‘theoretical’ here accounts for the increase of the spherical aberration and the deterioration of the beam propagation factor when a focusing lens of shorter focal length is used, therefore d_{f0} and Z_R do not decrease so sharply, and the same happens when a beam expander is incorporated; these are analysed by Harp’s article [2].

Where is the significance of these factors? The smaller the spot size, the more concentrated the energy, allowing for a greater machining speed, but as the Rayleigh length also gets shorter, only thinner material can be machined this way. When it comes to cutting pipes, one application being the cutting of coronary stents, wall thickness is small, therefore a small spot size may be used, and the advantage of the small Rayleigh length in this case will be of defocusing the laser on the pipe side opposite to cutting, i.e. it will be diverged, causing no or less heat-induced transformation in the opposite wall of the pipe (Figure 3).

The effect of changing different lenses in the case of an identical resonator is well demonstrated by Harp’s article [2]. Harp uses a 300 W, continuously operated ytterbium fibre laser resonator by IPG, first changing the focusing lens without

beam expander, trying lenses of focal lengths of 60, 100 and 150 mm in succession, thus changing the spot size of the focused laser beam from 18.9 micrometres (for a 60 mm focusing lens) to 48.7 micrometres (for a 150 mm focusing lens). We have calculated the Rayleigh lengths: these range from 253 micrometres (for a 60 mm focusing lens) to 1582 micrometres (for a 150 mm focusing lens) (Figure 4). The diameter of the beam delivery optical fibre was 9 micrometres with the wavelength of laser radiation being 1075 nm, which is advisable to be substituted in the formula in micrometres. The data of the focused beam cross-section with the calculated Rayleigh lengths are shown in Table 2, with the data of the experiment and the laser equipment shown in Table 3.

In the article the change of the parameters of the focused laser beam is even more pronounced when inserting a five-fold beam expander. Thus, the spot size of the focused laser beam changes from 9.36 micrometres (for a 100 mm focusing lens) to 11.5 micrometres (for a 150 mm focusing lens). This means that the size of the smallest achievable focal spot is about half as big when a beam expander is used than without a beam expander. It must be noted that the free cross-section of the lens only allowed a 4-fold beam expansion with a 60 mm focusing lens. We have calculated the Rayleigh lengths: these range from 36.9 micrometres (for a 60 mm focusing lens) to 76.7 micrometres (for a 150 mm focusing lens) (Figure 5). Therefore, using a beam expander, it is possible to reduce the Rayleigh length even to one-sixth of its size, compared to the case when it is not used.

The focal length of the collimator lens - the figure for which is missing from the article - can be determined by rearranging formula (4) making $f_{c,oll}$ the subject of it. It turned out to be 28.4 mm (8) for every optical element that was tested in the article.

A particular feature of Harp's article [2] [2] is that it determined the focal spot diameter and the beam propagation factor by a series of welding seams on a sample of Al-7075 T6 material positioned before the laser at an angle, while varying the optical elements in the laser head.

In Baumeister's article [6] the following data can be found: the focal spot diameter is 20 micrometres, the wavelength of laser radiation is 1090 nm, the beam quality factor is 1.1 and the diameter of the parallel beam before the focusing lens is 5 mm, there was no beam expander, therefore the value of B_e is 1. Based on this, rearranging and

making the focal length of the focusing lens the subject of formula (1), (5):

$$f = \frac{d_{f0} B_e d_b \pi}{4 \lambda M^2} \tag{5}$$

$f = 65,5$ mm is obtained. Notice that the formula

Table 2. The data provided in Harp's article and the results I have calculated

f (mm)	d_{f0} (mm)	B_e	Z_R (mm)	M^2
60	18,99	1	253,19	1,04
100	31,65	1	703,31	1,04
150	47,47	1	1582,45	1,04
60	11,08	4	36,93	2,43
100	9,36	5	41,60	1,54
150	11,50	5	76,67	1,26

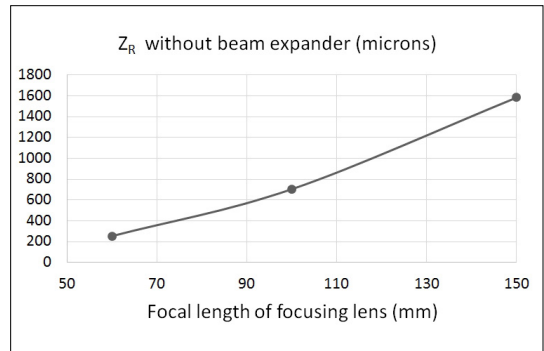


Figure 4. Change of the Rayleigh length as a function of the focal length of the focusing lens, without beam expander.

Table 3. Other data of the experiment and the laser experiment

Parameter	Value
d_{fc} (mm)	9
l (mm)	1,075
d_b (mm) unexpanded beam diameter	4,5
Manufacturer of laser equipment	IPG
Type of laser equipment	300 W, CW, ytterbium fibre laser
Machined material	Al-7075 T6
Thickness and geometry	Seams on top of the plate
Objective	Determination of laser beam cross-section near the focal point
Operation	Welding

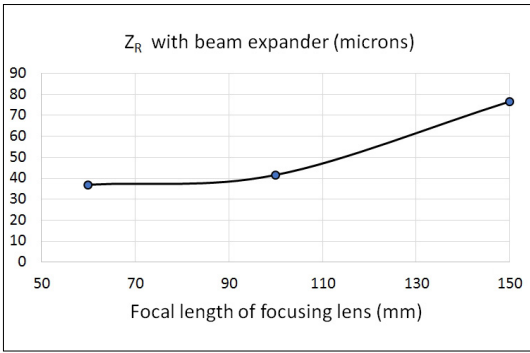


Figure 5. Change of the Rayleigh length as a function of the focal length of the focusing lens, with beam expander.

for focal spot diameter (1) only has to be multiplied by $f/(B_e d_b)$ to obtain the Rayleigh length from formula (2), that is (6):

$$Z_R = \frac{f}{B_e d_b} \tag{6}$$

A value of 262 micrometres is thereby obtained for Z_R . Since only a single fibre diameter is given, which is presumably that of the resonator, the focal length of the collimator cannot be calculated. The provided and calculated data are given in column 2 of **Table 4.** with the calculated values indicated by shaded backgrounds. The data of the laser and the machining are shown in column 2 of **Table 5.**

In Sobih’s article [7] the focal spot diameter is 73 micrometres, the focal length of the focusing lens is $f=190,5$ mm, the wavelength of laser radiation is 1090.5 nm, the beam quality factor is 1.1, with no beam expander used, therefore the value of B_e is 1. Based on this, formula (1) yields the diameter of the collimated beam before the focusing lens (7):

$$d_b = \frac{4\lambda M^2 f}{B_e d_{f0} \pi} \tag{7}$$

Using this result of 3,9 mm, the Rayleigh length is determined from formula (6) as approximately 3.5 mm. As the core diameter of the laser beam delivery optical fibre is given as 14 mm, the focal length of the collimator lens can be calculated from formula (3), to be 36 mm (8).

$$f_{coll} = \frac{d_{fc} f}{d_{f0}} \tag{8}$$

The provided and calculated data are given in column 3 of **Table 4.** with the calculated values indicated by shaded backgrounds. The data of the laser and the machining are shown in column 3

Table 4. The lasers examined and the machining data

Article	Baumeister 2006 [6]	Sobih 2007 [7]	Guerra 2019 [8]	Meszlényi 2019 [9]
d_{f0} (mm)	20	73	150	14
d_{fc} (mm)	n.a.	14	150	50
f (mm)	65,5	190,5	50	50
f_{coll} (mm)	n.a.	36	50	50
l (mm)	1,09	1,07	1,08	1,07
M^2	1,1	1,1	1,1	1,1
d_b (mm)	5	3,9	0,5	5,4
Z_R (mm)	262	3554	14867	131

Table 5. The lasers examined and the machining data

Article	Baumeister 2006 [6]	Sobih 2007 [7]
Manufacturer of laser equipment	SPI	IPG
Type of laser equipment (all fibre lasers)	SP-100 C single-mode 100 W	YLR- 1000-SM ytterbium
Machined material	1.4301	EN 43 annealed steel
Thickness and geometry	100...300 micrometres foil	1 mm plate
Operation	foil cutting	plate cutting
Objective	narrow cutting slit: achieving a width of 20 micrometres	achieving a smooth edge of cut

Table 6. The lasers examined and the machining data

Article	Guerra 2019 [8]	Meszlényi 2019 [9]
Manufacturer of laser equipment	Rofin	IPG
Type of laser equipment (all fibre lasers)	FL x50s	YLR-150/1500-QCW-AC-Y11
Machined material	316 stainless steel	copper and silver foil
Thickness and geometry	pipe	50 μm copper foil, 150 μm silver foil
Operation	cutting	drilling
Objective	stent cutting	examination of drilling strongly reflective materials

of **Table 5**.

In Guerra's article [8] the diameter of the beam delivering optical fibre is given as 150 micrometres, the focal length of the collimator lens as 50 mm and the focal length of the focusing lens as 50 mm, and therefore the focal spot diameter can be determined from formula (3) to be 150 micrometres. Based on this and the wavelength and beam quality factor given in **Table 4**, the Rayleigh length can be calculated from formula (6) to be approximately 15 mm (no beam expander was used, hence the value of $B_e = 1$). Using the data obtained so far, formula (7) yields the diameter of the collimated beam before the focusing lens as 0.5 mm. The provided and calculated data are given in column 4 of **Table 4**, with the calculated values indicated by shaded backgrounds. The data of the laser and the machining are shown in column 2 of **Table 6**.

In Meszlényi's article [9] the diameter of the beam delivering optical fibre is given as 14 micrometres and the focal length of the collimator lens expanding and collimating the exiting beam is 50 mm. The focal length of the lens focusing the collimated laser beam onto the workpiece is 50 mm (f). The position of the beam expander was 1, so the multiplication factor of the beam expansion factor (B_e) is 1, and the focal spot diameter from formula (4) is determined to be 14 micrometres. Based on this and the wavelength and beam quality factor given in **Table 4** the beam diameter before the focusing lens is determined as 5.4 mm using formula (7). Finally, the Rayleigh length can be calculated from formula (6) to be approximately 131 μm . The provided and calculated data are given in column 5 of **Table 4**, with the calculated values indicated by shaded backgrounds. The data of the laser and the machining are shown in column 3 of **Table 6**.

For all the articles analysed the machined material thickness was within the depth of focus, i.e. within the double of the Rayleigh length.

3. Conclusions

In our article we have presented the method of determining the missing data from scientific publications of material machining fibre lasers, through the combined use of formulae found in various parts of the available literature. These

data determine - from the exit of the optical fibre delivering the beam to the focal spot - the optical system shaping the beam placed in the machining head, and allow calculation of up to 3 of 8 missing data described in **Table 4**.

In our work the calculation of the missing factors according to various patterns, such as the focal length of the focusing lens, the focal length of the collimator, the diameter of the collimated beam, a focal spot diameter and the Rayleigh length has become possible. We have analysed the effect of changing the properties of the optical elements in the machining head on the focal spot diameter and the Rayleigh length.

References

- [1] Kaplan A. F.: *Theoretical Analysis of Laser Beam Cutting*. Shaker Ver. Aachen, 2002.
- [2] Harp W. R., Paleocrassas A. G., Tu J. F.: *A Practical method for determining the beam profile near the focal spot*. Int. J. Adv. Manuf. Technol., 37/11–12. (2008) 1113–1119. <https://doi.org/10.1007/s00170-007-1067-z>
- [3] Formulary. (accessed on Aug. 11, 2022). <https://www.silloptics.de/en/service/sill-technical-guide/laser-optics/formelsammlung>
- [4] Van Gemert R., Schoenly J., Sarrafi R., Mendes M.: *Fiber laser micromachining in high-volume manufacturing*. Industrial Laser Solutions, May, 2015.
- [5] Tu J. F., Paleocrassas A. G.: *3 Low speed laser welding of aluminium alloys using single-mode fiber lasers*. In: (szerk.: Xiaodong Na, Stone) *Laser Welding*, Ed. Rijeka, Croatia: SCIYO, 2010. 47–106. <https://doi.org/10.5772/9857>
- [6] Baumeister M., Dickmann K., Hoult T.: *Fiber laser micro-cutting of stainless steel sheets*. Applied Physics A, 85/2. (2006) 121–124. <https://doi.org/10.1007/s00339-006-3687-9>
- [7] Sobih M., Crouse P. L., Li L.: *Striation-free fibre laser cutting of mild steel sheets*. Applied Physics A, 90/1. (2008) 171–174. <https://doi.org/10.1007/s00339-007-4247-7>
- [8] Guerra A. J., Ciurana J.: *Minimum Quantity Lubrication in Fibre Laser Processing For Permanent Stents Manufacturing*. Procedia Manufacturing, 41. (2020) 492–499. <https://doi.org/10.1016/j.promfg.2019.09.036>
- [9] Meszlényi G., Bitay E.: *The Role of Focus Position in Single Pulse Laser Drilling of Highly Reflecting Materials*. Acta Materialia Transylvanica, 2/1. (2019) 61–68. <https://doi.org/10.33924/amt-2019-01-10>

Application of Artificial Neural Networks in Adsorption Studies. A case study

Norbert-Botond MIHÁLY,¹ Alexandra CSAVDÁRI²

1Faculty of Chemistry and Chemical Engineering, Babeş–Bolyai University, Cluj-Napoca, Romania,

¹norbert.mihaly@ubbcluj.ro

²alexandra.csavdari@ubbcluj.ro

Abstract

The work focuses on the development of an artificial neural network (ANN) based model that can describe the adsorption of benzalkonium chloride from aqueous solutions onto commercially available kitchen paper. Various ANN architectures were tested in order to find the most suitable one in terms of overlapping between calculated and measured output data (coefficient of determination and mean absolute percentage error), as well as correctly interpolating outputs when using inputs from inside the experimental training range. The networks all had 4 inputs and 1 output, as well as a single hidden layer. Optimal ANN design was sought by varying both the number of neurons in the hidden layer and the type of transfer function towards it. The best find was employed in assessing the relative importance of input parameter values in the output, as well as the model's suitability for predictions outside the training range.

Keywords: *benzalkonium chloride, adsorption, modelling, artificial neural networks.*

1. Introduction

Due to the recent pandemic, attention has shifted to studying active ingredients in disinfectants. Due to antibacterial activity, hand sanitizers containing benzalkonium chloride (BAC) were recommended by the CDC and WHO, as an alternative to alcohol-based products [1–3].

The intensive use of BAC products is risky, for example its accumulation in different environments may cause environmental damage. High concentrations of BAC affect aquatic ecosystems due to endocrine disruption in fishes, while long-term consequences are still the subject of further research [4]. BAC also influences microorganism activity in soil, hence their nitrogen transformation capacity [5], while in plants it can induce nutrient deficiency [6]. Although levels of BAC concentrations are regulated, this chemical species still raises concerns due to the limited understanding of its long term effects [7].

Adsorption is commonly used for the removal of pollutants from aqueous solutions. Adsorbents such as natural clays [8, 9] and polyethylene microplastics [10] were reported. The current study

employs household items (soft paper) as un-modified adsorbent material.

The complexity of the adsorption process and its dependence on several factors, such as: the type of adsorbent, temperature, mixing rate, mass ratio between adsorbed species and adsorbent, turns its modelling to a challenging task. An alternative to the traditional mathematical description of a process is the use of data-driven models, such as artificial neural networks (ANNs). Examples of their successful application in modelling adsorption have been reported for methylene blue [11], as well as sunset yellow [12]. In both cases ANN models gave accurate predictions in-between the experimental data points. Other studies used networks either for the design and optimization of a cyclic adsorption process [13], or for the determination of thermodynamic parameters in the adsorption of different ions [14].

The current study aims to model the adsorption of BAC on paper towels, thus removing it from aqueous solutions, by developing a suitable ANN. To the best of the authors' knowledge, this kind of modelling has not yet been applied either for

the BAC adsorption, or for the use of such a readily available adsorbent material. The benefits of such a network are: it could help the optimization of BAC removal by means of adsorption, be further used for forecasting, and lead to a better understanding of the underlying processes.

2. Materials and methods

2.1. Experimental database

Experimental data used to develop the ANN's were obtained during the laboratory scale adsorption of BAC on commercial paper towels. Absorbance of the aqueous BAC-paper mixtures were measured at 262 nm, resulting in values between 0.162 and 1.164. Experiments involved measurements at various temperatures (from 18 to 45 °C), initial BAC concentrations of the aqueous solution (from 0.25 to 1.00 g_{BAC}/L), and mass ratio values (from 25 to 100 mg_{BAC}/g_{adsorbent}).

2.2. Artificial neural networks

A feedforward artificial neural network architecture was taken into consideration for modeling this particular adsorption process. It is also known as multi-layer perceptron (MLP). Input data were provided by the experimental values of total liquid-solid contact time, temperature, initial BAC concentration and mass ratio, while the output of the model was set as the experimental absorbance value. In order to develop an accurate model, the optimal architecture for the MLP was sought by varying the number of neurons in the hidden layer, as well as the type of transfer function to the hidden layer. The first varied from 5 to 15. The latter was either a logarithmic sigmoid function (*logsig*), or a tangent sigmoid function (*tansig*). Transfer functions towards the output layer were always of linear (*purelin*) type.

The networks were trained using the Levenberg-Marquardt training algorithm. The database was divided as follows: 60% for the purpose of training, while 20% and 20% for validation and testing, respectively. All combinations of neuron numbers and transfer functions were developed, and the models were evaluated by two criteria: the value of the coefficient of determination (R^2) described by Eq. (1) and the value of the mean absolute percentage error (MAPE) shown in Eq. (2):

$$R^2 = 1 - \frac{\sum_{i=1}^N (y_i - x_i)^2}{\sum_{i=1}^N (y_i - \bar{y})^2} \quad (1)$$

$$MAPE = \frac{\sum_{i=1}^N \frac{|y_i - x_i|}{y_i}}{N} \cdot 100 \quad (2)$$

where N is the number of data points, y_i is the desired output at data point i , x_i is the ANN model output (prediction) at data point i , and \bar{y} is the mean of the (y_i) values (y_i and x_i are non-scaled values).

Models exhibiting both R^2 close to 1 and MAPE less than 3 were considered accurate enough for further simulations and applications.

3. Results and discussion

3.1. ANN development

From the total of 297 data points 177 were utilized for training, 60 for validation, and 60 for testing. The training for each architecture was repeated 5 times in order to reduce the impact of random initialization of network weights. The values of the mentioned criteria on the testing dataset are presented in **Table 1** for the best network from the five repetitions and for each architecture, when using a *logsig* transfer function. **Table 2** contains the same information, but for networks employing a *tansig* transfer function.

Results considered best are highlighted in the tables. All models show good and somewhat comparable R^2 values, while a *logsig* architecture (**Table 1**) with 9 neurons and a *tansig* one (**Table 2**) with 10 hidden neurons displayed the lowest MAPE values.

In order to decide on the best developed model which could be suitable for further simulations, their interpolation capability was tested. The model with a *logsig* transfer function is referred to as ANN 1, and the one with a *tansig* transfer function as ANN 2.

Table 1. Evaluation criteria results for ANN models of *logsig* architectures

Hidden neurons	MAPE	R^2
5	3.40	0.991
6	3.24	0.993
7	4.03	0.988
8	3.32	0.991
9	2.82	0.994
10	4.08	0.990
11	3.79	0.989
12	4.50	0.985
13	4.65	0.980
14	3.74	0.987
15	5.04	0.983

Table 2. Evaluation criteria results for ANN models of tansig architectures

Hidden neurons	MAPE	R ²
5	3.81	0.987
6	3.72	0.992
7	3.66	0.987
8	3.82	0.987
9	3.28	0.995
10	3.00	0.990
11	5.29	0.976
12	3.58	0.991
13	3.12	0.993
14	3.42	0.990
15	3.08	0.987

Figures 1a)–1c) illustrate the results of interpolation. The experimental data are represented as a scatter series, while the ANN-derived interpolated series are shown as scatter points connected by lines. The latter correspond to calculated output data obtained by averaging two experimental sets of input data. It is important to mention that only the parameters aimed for interpolation were varied.

It can be observed that ANN 2 shows better performance in case a), for temperature interpolation, as well as in case c), when both temperature and mass ratio interpolation was aimed for. In both cases ANN 1 underestimates the absorbance values, thus does not perform well. Hence, ANN 2 was chosen for further applications.

3.2. ANN model applications

A model corresponding to the architecture and interpolation capacity of ANN 2 was used to investigate the relative weight (importance) of input parameters in its output value, as well as for testing the forecasting ability of the model outside the range of training data.

3.2.1. Relative importance of input data

The relative importance (weight) of input variables was calculated by means of a method described by Gevrey et al [15]. This procedure uses the ANN model's connection weights for calculus. Table 3. contains the obtained results.

Results show that the total contact time between the liquid and the adsorbent is the most influential parameter for the investigated process, a finding that was expected. The second strongest

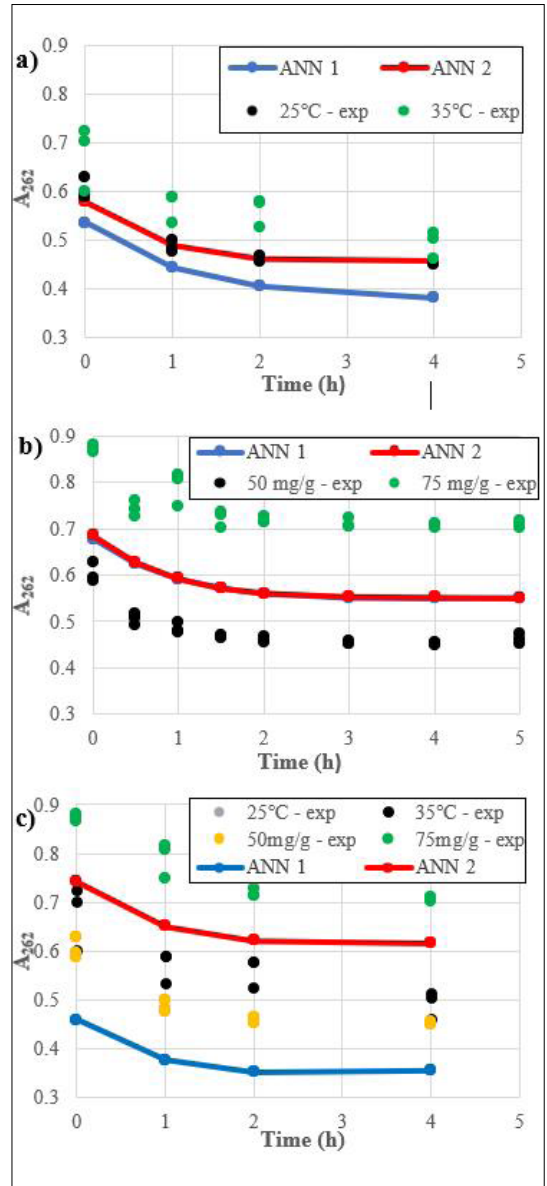


Figure 1. Interpolation results of the two ANN models for: a) temperature interpolation; b) BAC/adsorbent mass ratio interpolation; c) both temperature and BAC/adsorbent mass ratio interpolation

Table 3. Relative importance of input parameters in the model's output value

Model	Time (h)	Temperature (°C)	BAC initial concentration (g/L)	BAC/adsorbent mass ratio (mg/g)
ANN2	34.0 %	15.7 %	22.9 %	27.4 %

variable influencing the output is the mass ratio of BAC and adsorbent. This leads to the understanding that changing the mass ratio is more influential on this adsorption process than changing the initial BAC concentration of the aqueous solution. Meanwhile, temperature proved to be the least influential.

3.2.2. Prediction capacity outside the range of training data

The ANN 2 model was used to predict output data when fed with inputs that exceeded the experimental range for one of the parameters (values are located outside the range of training data). The aim was to test whether the forecasting can be trusted, and the developed model is still suitable for a mass ratio of BAC and adsorbent reaching $120 \text{ mg}_{\text{BAC}}/\text{g}_{\text{adsorbent}}$. Simulated results were compared to experimental values for $100 \text{ mg}_{\text{BAC}}/\text{g}_{\text{adsorbent}}$ (see Figure 2). The results show good agreement with the experimental data in terms of the variation of the absorbance in time, however a new set of experiments would be needed to truly validate the simulated values. Since the simulated series is not above the experimental data, which is to be expected based on the trend also shown in Figure 1b) these kinds of forecasts ought to be handled with caution.

4. Conclusions

Artificial neural network based models were developed to describe the adsorption of BAC on paper towels, resulting in accurate networks that exhibited MAPE values of 3 (or lower), together with R^2 values close to 1. The best architecture model was selected, not only based on the two performance criteria, but also taking into account the interpolation capability of it inside the range of training data. The selected model was further employed to determine the relative importance of input variables in the efficacy of an adsorption process. The latter is evaluated in agreement with the absorbance of the bulk phase absorbance of an aqueous BAC-paper mixture.

Other than time, the most important variable were found to be the mass ratio between BAC and the adsorbent, while temperature was the least influential parameter. Forecasting of absorbance using input data outside the training range was attempted for values exceeding just 20% of the upper limit, with fairly good overlap between the predicted and existing experimental outcomes.

Hence, the hereby developed model seems to be suitable for further applications, such as: forecast-

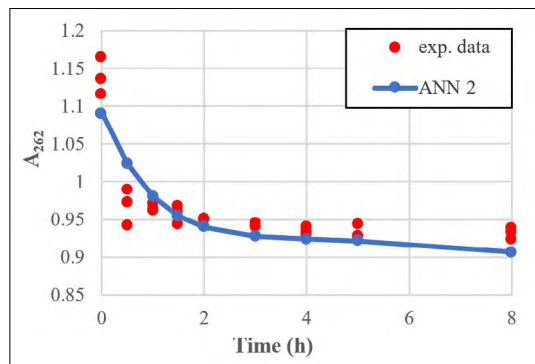


Figure 2. Time series of predicted $120 \text{ mg}_{\text{BAC}}/\text{g}_{\text{adsorbent}}$ mass ratio (ANN 2) vs. experimental series (exp. data) for $100 \text{ mg}_{\text{BAC}}/\text{g}_{\text{adsorbent}}$ mass ratio

ing of unknown scenarios and/or optimization of the adsorption process in question, but only within the range of the training (experimental) data.

References

- [1] Herdt B. L., Black E. P., Zhou S. S., Wilde C. J.: *Inactivation of SARS-CoV-2 by 2 commercially available Benzalkonium chloride-based hand sanitizers in comparison with an 80% ethanol-based hand sanitizer*. Infection Prevention in Practice, 3. (2021) 100191. <https://doi.org/10.1016/j.infpip.2021.100191>
- [2] Aodah A. H., Bakr A. A., Booq R. Y., Rahman M. J., Alzahrani D. A., Alsulami K. A., Alshaya H. A., Alsuabeyl M. S., Alyamani E. J., Tawfik E. A.: *Preparation and evaluation of benzalkonium chloride hand sanitizer as a potential alternative for alcohol-based hand gels*. Saudi Pharmaceutical Journal, 29. (2021) 807–814. <https://doi.org/10.1016/j.jsps.2021.06.002>
- [3] Ogilvie B. H., Solis-Leal A., Lopez J. B., Poole B. D., Robison R. A., Berges B. K.: *Alcohol-free hand sanitizer and other quaternary ammonium disinfectants quickly and effectively inactivate SARS-CoV-2*. Journal of Hospital Infection, 108. (2021) 142–145. <https://doi.org/10.1016/j.jhin.2020.11.023>
- [4] Kim S., Ji K., Shin H., Park S., Kho Y., Park K., Kim K., Choi K.: *Occurrences of benzalkonium chloride in streams near a pharmaceutical manufacturing complex in Korea and associated ecological risk*. Chemosphere, 256. (2020) 127084. <https://doi.org/10.1016/j.chemosphere.2020.127084>
- [5] Yang R., Zhou S., Zhang L., Qin C.: *Pronounced temporal changes in soil microbial community and nitrogen transformation caused by benzalkonium chloride*. Journal of Environmental Sciences, (2022). <https://doi.org/10.1016/j.jes.2022.04.004>

- [6] Khan A. H., Libby M., Winnick D., Palmer J., Sumarah M., Ray M. B., Macfie S. M.: *Uptake and phytotoxic effect of benzalkonium chlorides in Lepidium sativum and Lactuca sativa*. Journal of Environmental Management, 206. (2018) 490–497. <https://doi.org/10.1016/j.jenvman.2017.10.077>
- [7] Pereira B. M. P., Tagkopoulos I.: *Benzalkonium chlorides: Uses, regulatory status, and microbial resistance*. Applied and Environmental Microbiology, 85. (2019) 1–27. <https://doi.org/10.1128/AEM.00377-19>
- [8] Zanini G. P., Ovesen R. G., Hansen H. C. B., Strobel B. W.: *Adsorption of the disinfectant benzalkonium chloride on montmorillonite. Synergistic effect in mixture of molecules with different chain lengths*. Journal of Environmental Management, 128. (2013) 100–105. <https://doi.org/10.1016/j.jenvman.2013.04.056>
- [9] Ndabambi M., Kwon J. H.: *Benzalkonium ion sorption to peat and clays: Relative contributions of ion exchange and van der Waals interactions*. Chemosphere, 247. (2020) 125924. <https://doi.org/10.1016/j.chemosphere.2020.125924>
- [10] Kim T. K., Jang M., Hwang Y. S.: *Adsorption of benzalkonium chlorides onto polyethylene microplastics: Mechanism and toxicity evaluation*. Journal of Hazardous Materials, 426. (2022) 128076. <https://doi.org/10.1016/j.jhazmat.2021.128076>
- [11] Ghosh I., Kar S., Chatterjee T., Bar N., Das S. K.: *Removal of methylene blue from aqueous solution using Lathyrus sativus husk: Adsorption study, MPR and ANN modelling*. Process Safety and Environmental Protection, 149. (2021) 345–361. <https://doi.org/10.1016/j.psep.2020.11.003>
- [12] Ahmad Z. U., Yao L., Lian Q., Islam F., Zappi M. E., Gang D. D.: *The use of artificial neural network (ANN) for modeling adsorption of sunset yellow onto neodymium modified ordered mesoporous carbon*. Chemosphere, 256. (2020) 127081. <https://doi.org/10.1016/j.chemosphere.2020.127081>
- [13] Pai K. N., Nguyen T. T. T., Prasad V., Rajendran A.: *Experimental validation of an adsorbent-agnostic artificial neural network (ANN) framework for the design and optimization of cyclic adsorption processes*. Separation and Purification Technology, (2022) 120783. <https://doi.org/10.1016/j.seppur.2022.120783>
- [14] Fagundez J. L. S., Netto M. S., Dotto G. L., Salau N. P. G.: *A new method of developing ANN-isotherm hybrid models for the determination of thermodynamic parameters in the adsorption of ions Ag⁺, Co²⁺ and Cu²⁺ onto zeolites ZSM-5, HY, and 4A*. Journal of Environmental Chemical Engineering, 9. (2021) 106126. <https://doi.org/10.1016/j.jece.2021.106126>
- [15] Gevrey M., Dimopoulos I., Lek S.: *Review and comparison of methods to study the contribution of variables in artificial neural network models*. Ecological Modelling, 160. (2003) 249–264. [https://doi.org/10.1016/S0304-3800\(02\)00257-0](https://doi.org/10.1016/S0304-3800(02)00257-0)

Investigation of Raw Materials for Sulfurized Vegetable Oil Based Lubricant Additives

Gábor Zoltán NAGY,¹ Nikoletta LÁZÁR,² Roland NAGY³

¹ University of Pannonia, Faculty of Engineering, Department of MOL Hydrocarbon and Coal Processing, Veszprém, Hungary, gznagy@phd.uni-pannon.hu

² University of Pannonia, Faculty of Engineering, Department of MOL Hydrocarbon and Coal Processing, Veszprém, Hungary, nikoletta.lazar96@gmail.com

³ University of Pannonia, Faculty of Engineering, Department of MOL Hydrocarbon and Coal Processing, Veszprém, Hungary, nroland@almos.uni-pannon.hu

Abstract

Extreme Pressure (EP) additives are commonly used in lubricants to reduce wear and prevent seizures at high temperature and pressure. In terms of their mechanism, these build up a film on the surface with chemisorption. This film efficiently prevents metal-metal adhesion. Industrial statistics show that extreme pressure additives are mostly used in metalworking fluids, lubricating greases and engine oils. Sulfurized vegetable oils can be used as EP additives of lubricants. This type of EP additive is ashless, derived from renewable sources and have a lesser negative effect on the environment compared to those that are not derived from vegetable sources. To determine the appropriate vegetable oils to be used as the raw material of EP additives, the structure of triglycerides, cost-effectiveness and availability aspects must be considered. Results of experiments show that rapeseed oil and soybean oil best meet this criteria system.

Keywords: *antiwear, vegetable oil, sulfurized oil, additive.*

1. Introduction

1.1. The EP-additives

Modern lubricants use different additives to improve their different properties or to give them a new, favourable property, thus meeting the quality requirements for the lubricant [1]. There are many types of additives, in addition to EP additives, there are detergent-dispersant additives, corrosion inhibitors, oxidation inhibitors, and others. The purpose of anti-wear and EP additives is to reduce wear and prevent seizures even at very high temperatures and pressures.

It is not entirely possible to distinguish between anti-wear and EP additives. The use of an additive in one case has an anti-wear effect, while the use of this additive in another case acts as an EP additive. There are also cases where both effects are exerted by a given additive. The mechanisms of action of the two additive types (Figure 1) are the same and can be grouped according to their ac-

tivity temperature. Anti-wear additives work at low temperatures, while EP additives work at higher temperatures [2].

EP additives are highly reactive, can impair the oxidation stability of the oil, cause corrosion in non-ferrous metals, and reduce the fatigue resistance of bearings and other equipment [3].

EP additives are designed to prevent metal-to-metal adhesion or welding if the natural protective oxide layer between the contact surfaces is removed and other active compounds in the oil are not reactive enough to prevent the protective film from disappearing. This is most often in the case of high-speed, high-load, and/or high-temperature operations [4, 5].

In terms of mechanism of action, these additives work by reacting with the surface of the metal to form a metal compound similar to anti-wear additives, but here the reaction rate is higher, the film formed is thicker and more resistant and the shear strength of the resulting film is lower than metal. EP additives can prevent scratches, abra-

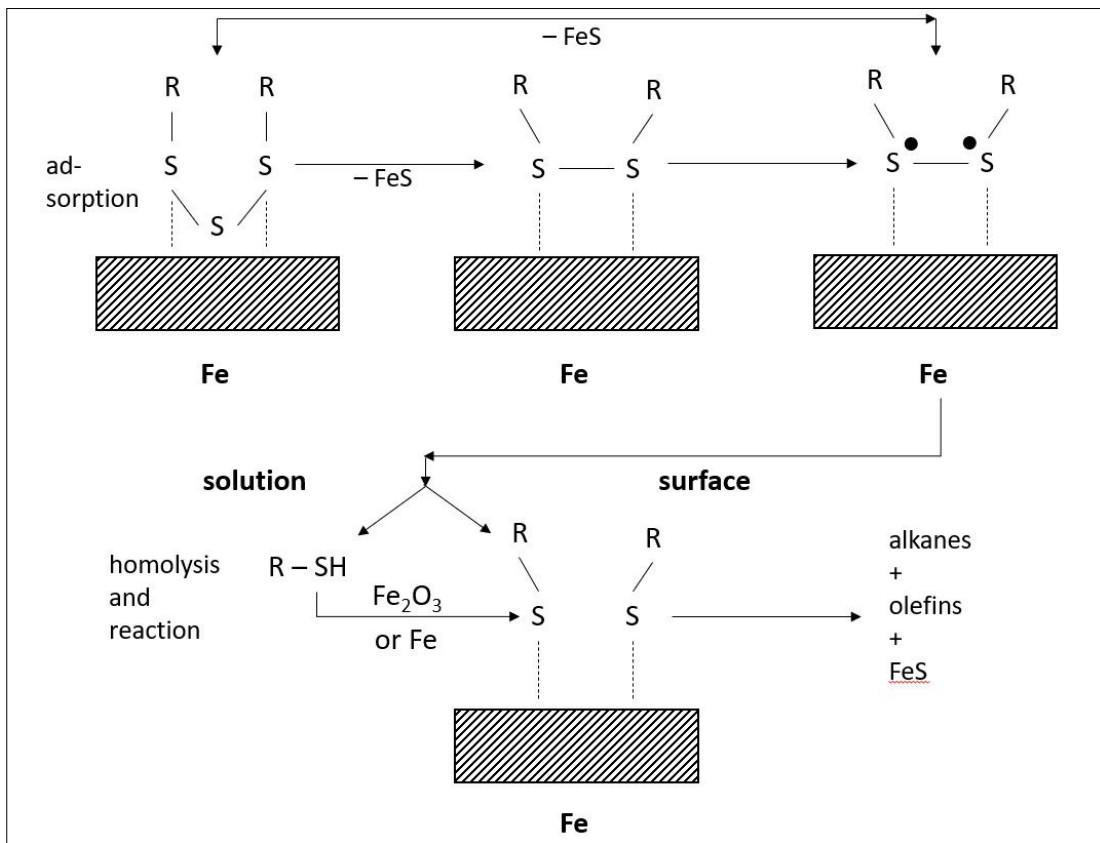


Figure 1. The mechanism of action of EP additives on iron metal surfaces.

sion and sticking under high speed and impact loads. During use, EP additives deplete and the surface of the metals wears evenly, resulting in a smoother surface, thus increasing the chances of hydrodynamic lubrication, resulting in less local stress and lower friction [4, 6].

Both anti-wear and EP additives are available in a wide range, but their selection must consider, among other things, economic considerations, the oil solubility, and the oxidative stability-reducing effect of the additive [4, 7].

The preparation of sulfurized EP additives requires, above all, a sulfurizable compound and a sulfurizing compound. The selectivity of the reaction can be improved by using a catalyst. Compounds containing one or more double bonds are used as sulfurizable compounds. These include vegetable oils, fatty acids and fatty acid esters, as well as olefins, acrylates and methacrylates. Orthorhombic elemental sulfur and hydrogen sulfide are widely used as sulfurizing compounds. In addition, other sulfur donors containing bounded

sulfur, such as mercaptans, can be used [1, 2, 4].

In the current phase of the research, we aimed to examine the range of vegetable oils that can be used for the production of sulfurized vegetable oil additives based on literature data and to compare them based on properties that have key importance for the synthesis of EP additives. Furthermore, our goal was to select vegetable oils that can be used with favourable results for the production of EP additives based on sulfurized vegetable oils.

1.2. Vegetable oil

The value and field of application of vegetable oils depend on their fatty acid composition, so since each vegetable oil has different physical and chemical properties, so does its field of application. For example, oils containing side chains with 12 carbon atoms (e.g. lauric acid) are important raw materials for the production of detergents and surfactants, while oils containing side chains with 18-22 carbon atoms (e.g. oleic acid)

are used in lubricants or as polymer additives [4, 8].

In terms of regions, the Asian market dominates both production and consumption. Rapeseed oil is the most widely used vegetable oil as a bio-lubricant on the European market, sunflower oil and soybean oil have greater importance in the US. In addition, the role of castor oil, corn oil and safflower oil are small [8].

Wax esters are oxo-esters of long-chain fatty acids and long-chain fatty alcohols. Wax esters of natural origin are mixtures of esters but also contain hydrocarbons. Wax esters have excellent performance properties due to their high oxidation stability and good resistance to hydrolysis. For this reason, stable additive compounds can be synthesized even under the conditions of the use of EP additives. The oxidation stability of each vegetable oil is illustrated in Table 1 [4, 8].

The linear structure gives the lubricant an anti-corrosion, anti-foaming, anti-wear and anti-friction effect. Due to these properties, they are excellent raw materials for high temperature and high pressure lubricants such as hydraulic fluids and EP additives. Wax esters are neutral lipids that are solid at room temperature and have limited availability in nature (cachaot oil, jojoba oil) [8].

2. Results

2.1. Investigation of vegetable oils that can be used as a raw material of EP additives

Glycerol esters of long-chain fatty acids can be used as raw materials for EP additives. Examples are white meadowfoam oil, rapeseed oil, Crambe tataria oil, soybean oil, peanut oil, sunflower oil,

Table 1. Comparison of oxidative stability index of some vegetable oils

Vegetable oil	Oxidation stability index at 110 °C
White meadowfoam oil	246.9
Refined white meadowfoam oil	67.3
Cold-pressed jojoba oil	55.9
Crude jojoba oil	34.5
Refined jojoba oil	31.4
Refined soybean oil	19.9
Refined castor oil	56.1

olive oil, corn oil, coconut oil and palm oil. In addition to triesters, monoesters such as jojoba oil, an ester of long unsaturated fatty acids and long unsaturated alcohols, can be used. Mixtures of triesters and monoesters can also be used. Non-edible raw materials (castor oil, white meadowfoam oil, Crambe tataria oil) enjoy a market advantage, both for economic and environmental reasons [8].

2.1.1. White meadowfoam oil

The white meadowfoam is a perennial plant native to the northwestern region of the United States. The oil is extracted from its seeds, which contain about 27% oil [9].

Crude white meadowfoam oil contains long-chain fatty acids ($\geq 97\%$ C20), making it a very stable and unique source of unsaturated long-chain fatty acids. Due to this unique chemical composition, many developments are underway to become an industrial oil crop. During its decomposition, monoene fatty acids are formed, which, for example, has an unusually high oxidation stability index compared to other vegetable oils, which is well illustrated in Table 1.

For this reason, it is recommended for areas that produce very valuable products [8].

However, the disadvantage of it is that the diene-structure causes solubility problems during sulfurization due to the formation of crosslinks. By sulfurizing the oil for two hours at 180°C with 20 % sulfur, the product is obtained almost insoluble in hydrocarbon oils [9].

2.1.2. Rapeseed oil

In terms of the composition of rapeseed oil, it consists of a high amount (about 60%) of mono-unsaturated oleic acid and a low amount (about 5.5%) of saturated fatty acids. The main disadvantage of rapeseed oils is their relatively high content of linoleic acid (C18: 2) and linolenic acid (C18: 3).

Rapeseed oil is excellent for use in biotechnological processes. The synthesis of oil in rapeseed can be influenced to produce specific, chemically modified triglycerides. Due to its high oleic acid content, it is a popular raw material in the food industry due to its good quality and low saturated fatty acid content [8].

2.1.3. Crambe tataria oil

Crambe tataria is a drought-tolerant, low-nutrient plant native to Ethiopia that has been grown and processed on an industrial scale in the U.S.

since 1990. The oil content of the seeds in the *Crambe tataria* is approx. 30% with a high erucic acid content (>50% C22:1) and a low free fatty acid content (<0.5%).

Refined *Crambe tataria* oil is mainly used as a source of erucic acid, but there is also a lot of research into its conversion to a wax ester (EPOBIO project), which could be used for lubrication purposes, including as a base for EP additives.

However, it contains large amounts of linoleic acid and linolenic acid, which negatively affect oxidation stability. Erucic acid has high viscosity but has a negative effect on cold flow properties due to its high melting point [8].

2.1.4. Jojoba oil

After the banning of sulfurized cachalot oil, there was a lot of research to replace it in the late 1970s. One way to replace cachalot oil is with jojoba oil, which has several benefits, such as a more pleasant smell than cachalot oil. Furthermore, crude jojoba oil does not contain glycerides, so fewer purification steps are required before use [9].

The jojoba plant is an evergreen shrub with tiny seeds. It is also used in many fields, such as the pharmaceutical industry, the cosmetics industry, and the production of biofuels. However, its disadvantage is that its annual production is 5 kilotons, which does not meet global trade needs [8].

Jojoba oil has a low or no glyceride chemical composition and most of its compounds have a carbon number between 36 and 42. This narrow carbon number range and linear structure give jojoba oil unique properties. So jojoba oil is a monoester with a high molecular weight and is made up of straight-chain fatty acids and fatty alcohols that also contain a double bond. The molecular structure is represented in Figure 2, in which m and n are between 8 and 12.

Jojoba oil is mainly a fatty acid ester of decyl alcohol. Its advantageous properties include its unusually high oxidation stability, especially at high temperatures. This has been shown to be due in part or whole to the tocopherol and other natural antioxidants it contains [10].

Soluble in organic solvents due to its physical properties, but not miscible with ethanol, methanol, acetic acid or acetone. A light golden, non-vol-

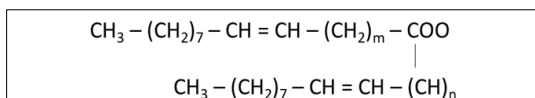


Figure 2. Molecular structure of jojoba oil

Table 2. Main properties of jojoba oil

Properties	Value	Test method
Density (g/cm ³)	0.863	ASTM D-1298
Refractivity index, n _D 20	1.4652	ASTM D-1218
Kinematic viscosity at 40 °C (cSt)	26	ASTM D-445
Kinematic viscosity at 100 °C (cSt)	7.5	ASTM D-445
Viscosity index	257	ASTM D-189
Acid number (mgKOH/g)	2.0	ASTM D-664
Flashpoint (°C)	310	ASTM D-92
Iodine value (g _{I₂} /100g)	80	ASTM D-2075
Average molecular weight (g/mol)	604	GPC

atile liquid with low acid content. Several other physical properties are summarized in Table 2.

2.1.5. Soybean oil

Soybeans are native to Northeast Asia, where the climate is temperate. Soybeans are sensitive to temperature changes and require four different seasons. Worldwide soybean cultivation is estimated at 257.5 million tons, and the main soybean-growing countries are the US and Argentina.

Refined soybean oil is a good lubricant but is not preferred for many applications because it oxidizes too quickly. This problem, and thus its short shelf life, can be eliminated in several ways, such as by chemical modification (partial hydrogenation and epoxidation), the use of additives, esterification with palm oil, or possibly mixing with jojoba oil. Jojoba oil is effective in reducing the formation of hydroperoxide and other volatile components in soybean oil, making any mixture of jojoba oil and soybean oil more stable than pure soybean oil. Mixing them in an 80:20 soybean oil:jojoba oil ratio is most effective for the oxidative stability of soybean oil [8].

2.2. Selection of vegetable oils that can be used as a raw material of EP additives

There are many types of vegetable oils, each with a different structure and thus different properties. Jojoba oil, white meadowfoam oil, rapeseed oil and *Crambe tataria* oil are the best criteria for the use of vegetable oils as EP additives, and soybean oil can also be used. However,

Table 3. Typical composition of investigated vegetable oils

Vegetable oil	Average fatty acid distribution of triglycerides that build up vegetable oils, %			
	< C18	C18	C20	C22 <
White meadow-foam oil	0.6	2.1	65.7	31.6
Rapeseed oil	4.8	88.1	2.4	4.7
Crambe tataria oil	3.6	34.3	10.7	51.4
Jjoba oil	1.8	78.5	0.2	19.5
Soybean oil	11.4	83.3	0.5	4.8

an examination of a mixture of these may give satisfactory results.

Based on the previous reference, triglycerides containing C18-C22 fatty acid chains can be advantageously used as a raw material for the synthesis of lubricant additives [4, 8]. Of the investigated vegetable oils, rapeseed oil, jojoba oil and soybean oil, which contain the highest proportion of triglycerides in this carbon number range, meet this condition the most. The average distribution of fatty acids found in the studied vegetable oils is shown in Table 3 [9, 10].

Among the studied vegetable oils, the composition of the previously used cachalot oil corresponds to the composition of jojoba oil, since it is similarly a wax ester, one of the properties of which is the high oxidation stability. However, the use of jojoba oil is neither advantageous nor economically advantageous.

Like jojoba oil, white meadowfoam oil and Crambe tataria oil are not available in sufficient quantities in Europe. However, the oil in the Crambe tataria would have to be converted to a wax ester to be used as a base for EP additive, which has additional costs.

The suitability of the investigated vegetable oils for synthesis and their evaluation from an economic point of view is briefly summarized in Table 4.

For these reasons, rapeseed oil and soybean oil, or a mixture of these, are expected to yield favourable results in our further research.

3. Conclusions

Based on the information available in the literature, we examined the range of vegetable oils

Table 4. Applicability of investigated vegetable oils

Vegetable oil	Suitability for EP additive synthesis	Regional availability	Raw material cost
White meadowfoam oil	Suitable	Difficult supply	High
Rapeseed oil	Excellent	Easily available	Low
Crambe tataria oil	Suitable	Difficult supply	High
Jjoba oil	Excellent	Difficult supply	High
Soybean oil	Excellent	Available	Medium

that are most suitable for the production of sulfur-based vegetable oil-based EP additives based on the published results.

Based on a review of the literature, the fatty acid components of vegetable oils that can be used as EP additives should have a carbon number of 18 to 22, and 90% of the fatty acids should preferably contain one but no more than three double bonds.

Based on the comparison of the results and taking into account the economics and availability conditions, we will use rapeseed oil and soybean oil, or a mixture of them, for the synthesis of EP additive samples in the next experimental phase of the research.

References

- [1] Theo M., Wilfried D.: *Lubricants and Lubrication*. Second Edition. Wiley, Weinheim, 2007. 88–119.
- [2] Syed Q. A. R.: *A Comprehensive Review of Lubricant Chemistry, Technology, Selection and Design*. ASTM International, West Conshohocken, PH, 2009. 149–181.
- [3] Pradeep L. M., Sudeep P. I., Michael N., Satish V. K., Michael R. L.: *Tribology for Scientists and Engineers*. Springer, New York, NY, 2013. 317–318.
- [4] Leslie R. R.: *Lubricant Additives. Chemistry and Applications*. Third Edition. CRC Press, Boca Raton, FL, 2017. 211–278.
- [5] Vámos E.: *Tribológiai kézikönyv. Gépek és gépelemek súrlódása, kopása, kenése*. Műszaki Könyvkiadó, Budapest, 1983. 36–116.
- [6] Theo M., Kirsten B., Thorsten B.: *Industrial Tribology. Tribosystems, Friction, Wear and Surface Engineering, Lubrication*. Wiley, Weinheim, 2011. 320–335.
- [7] Don M. P., Martin W., Ekkehard D.: *Lubrication Fundamentals*. Third Edition. CRC Press, Boca Raton, FL, 2016. 35–60.

- [8] Theo M.: *Encyclopaedia of Lubricants and Lubrication*. Springer, Berlin, 2014. 131–146.
- [9] Frank L. E., Phillip S. L., Robert E. A.: *Vegetable oil derivatives as lubricant additives*. EP0353872A1, USA, 1979.
- [10] Edward W. B.: *Wax esters of vegetable oil fatty acids useful as lubricants*. US4152278, USA, 1979.

Analysis of the Harmful Effects of UV Radiation Generated During Welding

Márton SCHRAMKÓ,¹ Abdallah KAFI,² Tünde Anna KOVÁCS³

¹ Óbuda University, Doctoral School on Materials and Materials Technology, Budapest, Hungary, schramko.marton@bgk.uni-obuda.hu

² Óbuda University, Doctoral School on Safety and Security Sciences, Budapest, Hungary, abdallahkafi1994@gmail.com

³ Óbuda University, Bánki Donát Faculty of Mechanical and Safety Engineering, Budapest, Hungary,, kovacs.tunde@bgk.uni-obuda.hu

Abstract

Arc welding produces several harmful health effects on the welder. The authors aimed to determine the intensity of ultraviolet (UV) radiation as a function of distance from the welding. The research focused on the UV radiation generated during the arc welding process as it is a widely used process in industrial practice today. During the experiment, several tests were performed on the gas metal arc welding process (GMAW). This procedure is also used automated in the industry, so research can help to designate a specific safety zone in an industrial area so that there is no need to separate the welder robot with a curtain, but at the same time be able to move around them. Where the production is not fully automated yet, it highlights the problems which cause possible damage to health and helps create safer working conditions.

Keywords: *ultraviolet radiation; arc welding; safety zone.*

1. Ultraviolet effects

Ultraviolet, in short, UV radiation, is electromagnetic radiation of a wavelength of between 100 and 400 nm (below that of visible light). The UV range can be further divided into UV-A between 315–400 nm, UV-B between 315–280 nm and UV-C between 280–100 nm [1]. The main source of UV radiation on earth is solar radiation. The largest amount of ultraviolet radiation which reaches the earth's surface is UV-A radiation, most of the UV-B and all of the UV-C are absorbed by the stratospheric ozone layer. However, during arc welding, the device emits the entire spectrum of UV [2].

UV radiation strongly interacts with the molecules that make up living organisms, damaging them, so increased exposure to UV radiation poses a serious health risk.

Well-known examples of its acute health effects include keratoconjunctivitis and erythema.

UV-C radiation is absorbed by the cornea, UV-B and UV-A radiation is also absorbed by the cornea

and the lens of the eye, and only a small amount of UV radiation reaches the retina [3]. Keratoconjunctivitis is an inflammatory condition of the cornea, which is associated with unpleasant symptoms, such as pain, the feeling of a foreign body in the eye, blurred vision, sensitivity to light, tearing and eyelid spasms. The symptoms will disappear within 2 days [4].

Erythema, i.e. skin redness, caused by UV radiation – is increased blood flow within the surface capillaries of the skin.

UV-B and UV-C radiation have a direct DNA-damaging effect. The body recognizes the damage and initiates several defence mechanisms, including DNA repair to reverse the damage, apoptosis and exfoliation to remove irreparably damaged skin cells, and increased melanin production to prevent future damage [5].

UV radiation can induce many chronic processes in the body.

UV-B and UV-C radiation damage DNA directly or indirectly together with UV-A by creating re-

active oxygen radicals. This causes premature skin ageing, loss of skin tone, and formation of wrinkles, metalloproteinases are induced, which cleave collagen, the structural protein that ensures the skin's elasticity [6].

Long-term exposure to UV radiation and the resulting DNA damage can have much more serious consequences than premature skin ageing. UV radiation is known to be carcinogenic, and damage and improper repair of special DNA sequences, so-called proto-oncogenes and immunosuppressor genes, can lead to the development of cancer [7].

UV radiation also induces immunosuppression, which aggravates the course of infectious diseases and further increases the likelihood of developing skin cancer [8].

UV radiation reaching the eyes is a serious risk factor for the development of serious diseases that cause vision loss, such as cataracts and macular degeneration [9].

1.1. Permissible level of UV radiation

The intensity of ultraviolet radiation to which a person can be exposed in a day is maximized by a given daily UV limit. According to the literature, this limit value is 3 mW/cm², which means that if the body receives a dose higher than this, it will eventually no longer be able to recover easily, thus increasing the degree of permanent damage to the cells. The example below can help to make it easier to interpret, if the UV measuring instrument measures a value of 0.001-0.002 mW/cm², it means that the person exposed to it can stay in the irradiated area for 30-60 minutes. This value can be modified based on whether the measured radiation falls into the UV-A, -B or -C range. Because different regions damage the body to different extents [3].

We can determine the intensity of ultraviolet radiation as a safety value that can be interpreted for the whole day. To calculate this, knowledge of the following formulas is required (1), (2):

$$E_{eff} = \sum_{180}^{400} E_{\lambda} \cdot S(\lambda) \cdot \Delta\lambda \quad (1)$$

$$t_{max} = \frac{3 \text{ mJ/cm}^2}{E_{eff}} \quad (2)$$

The first formula gives the radiation efficiency. The second is the daily limit of UV radiation. In the formula for the efficiency of radiation, letters mean the following: E_{λ} special radiation, W/(cm²·nm); $S(\lambda)$ relative spectral efficiency;

$\Delta\lambda$ is the center wavelength, nm. In the second formula, the value of 3 mJ/cm² corresponds to the daily permissible value. We can interpret this as being exposed to 3 mW/(cm²·nm) UV radiation for 1 second during a day without harmful effects [10].

The exposure accumulates during the day and can quickly reach the limit without any protective equipment. It is worth mentioning here that as radiation spreads in the air, the amount of radiation decreases significantly depending on the distance. Also, during welding, the emission of the arc light wavelength changes as a function of the medium (shielding gas), according to the range in which the medium emits invisible or visible light [3].

2. Experiment

In the case of arc welding, UV radiation is an unavoidable source of inherent danger. For this reason, protective equipment is currently defined, for example: as covering skin surfaces with clothes or welding masks, shields or protective glasses. This protective equipment has been in use for many years and mainly focuses on absorbing and blocking UV light and only protects the wearer directly. In the welding halls, the individual welding stations are separated by curtains and screens, thus protecting the other welders. Our suggestion arose from the fact that knowing the given radiation intensity, a safety zone can be created while there is no need to completely cover the stations and workers could be able to walk between the welding robots following the designated routes without wearing protective gear.

2.1. The course of the experiment

Several articles have already been published in connection with this measurement. Our main goal is to measure the amount of ultraviolet radiation emitted during a given time and with the help of this, depending on the distance, specify a daily maximum value to which the body can be exposed. Adherence to this amount is important, as ignoring the recommendation can easily cause the problems described in the first part of this article.

The measurement was carried out with the help of a welding machine, on which both the welding values and the selection of gas mixtures could be easily controlled. The experiment aimed to define the effect of different gas mixtures on UV emission. Figure 1. shows a schematic representation of the experiment.

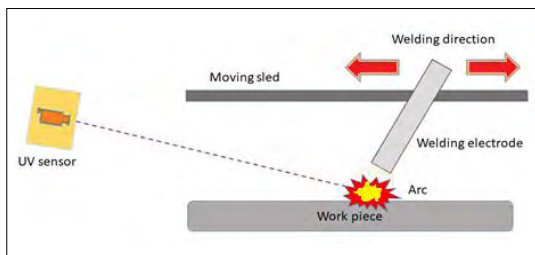


Figure 1. Schematic diagram of the measurement.

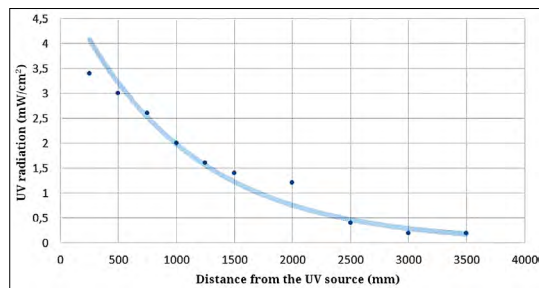


Figure 2. Diagram of UV intensity as a function of distance.

Table 1. UV data as a function of distance

Distance (m)	0.5	1	1,5
UV radiation mW/(cm ² -nm)	1.1–2.3	0.34–0.6	0.095–0.2

During the measurements, we established that the individual shielding gas mixtures can influence the amount of ultraviolet radiation, but the exact measurement evaluations are still in progress. In addition, we carried out measurements to see how the UV emission might change in the case of other welding processes, and it was interesting to observe that in the case of TIG welding, with the same material and protective gas, we were able to measure much lower values, which is a positive thing, since this process is still a very widely used procedure performed by humans.

To be able to quantify our results further, **Table 1** contains some measurement results. The measurement was made from several points and the distance changed due to the movement of the arc, so the values obtained are displayed as a range. The propagation of light can be demonstrated with the help of these data. The gas that we used as a shielding gas for the test was carbon dioxide (CO₂) which was carried out on S235 steel with SG2 yield material, with a feed of 7 m/min and a shielding gas dosage of 18 l/min and with the use of 171 A current.

The results clearly show how large a change in the intensity of ultraviolet radiation occurs depending on the distance. As the radiation spreads through the medium (air), it loses its ability to cause damage relatively quickly, so if the distances are correctly marked, the problem can be easily dealt with.

Searching the literature, we found a study where small experiments were carried out with the same shielding gas, and I would like to compare our results with them. The results of the research team “O., E. Otokpa, Y. B Usman” are shown in **Figure 2** [11].

Although the diagram was made from experimental data with a similar shielding gas, the current used was higher. Thus, the nature of the UV propagation can be read from the diagram, but it is not fully compatible with our results.

3. Conclusions

Based on the current results of our research, we can say that the results of the trials support the proposition that depending on the distance, we can create a specific safety zone based on a knowledge of the shielding gas and the welding process. However, to determine the zone, it is necessary to know how much time a given worker will spend walking between the machines because even at a distance of 2.5 m, he can only spend a relatively small amount of time near the machines. In our opinion, perhaps it would be worthwhile to create a model with the placement of the machines, which makes it possible to calculate the route together with the speed of travel since on a large section of the route it would be further away.

References

- [1] Gallagher R. P., Lee T. K., Bajdik C. D. & Borugian M.: *Ultraviolet radiation*. Chronic diseases in Canada, 29/1. (2010) 51–68. <https://doi.org/10.24095/hpcdp.29.S1.04>
- [2] Dixon A. J. & Dixon B. F.: *Ultraviolet radiation from welding and possible risk of skin and ocular malignancy*. Medical Journal of Australia, 181. (2004) 155–157. <https://doi.org/10.5694/j.1326-5377.2004.tb06207.x>
- [3] Takahashi J., Nakashima H., Fujii N., Okuno T.: *Comprehensive analysis of hazard of ultraviolet radiation emitted during arc welding of cast iron*. Journal of Occupational Health, 62. (2019) 1–10. <https://doi.org/10.1002/1348-9585.12091>
- [4] Hussey M., Wu B., Moore L. A. & Ferrreira J. T.: *Review of photokeratitis : Corneal response to ultraviolet radiation (UVR) exposure*. African Vision and Eye Health, 69. (2010) 123–131. <https://doi.org/10.4102/aveh.v69i3.137>

- [5] Sklar L. R., Almutawa F., Lim H. W. & Hamzavi I.: *Photochemical & Photobiological Sciences*. Photochemical & Photobiological Sciences, 12. (2013) 54–64.
- [6] Berneburg M., Plettenberg H. & Krutmann J.: *Photoaging of human skin*. Photodermatology, Photoimmunology and Photomedicine, 16. (2000) 239–244.
- [7] Narayanan D. L., Saladi R. N., Fox J. L.: *Ultraviolet radiation and skin cancer*. International Journal of Dermatology, 49. (2010) 978–986.
<https://doi.org/10.1111/j.1365-4632.2010.04474.x>
- [8] Norval M., Halliday G. M.: *The Consequences of UV-Induced Immunosuppression for Human Health*. Photochemistry and Photobiology, 87. (2011) 965–977.
<https://doi.org/10.1111/j.1751-1097.2011.00969.x>
- [9] Roberts J. E.: *Ultraviolet Radiation as a Risk Factor for Cataract and Macular Degeneration*. Eye & Contact Lens: Science & Clinical Practice, 37. (2011) 246–249.
<https://doi.org/10.1097/ICL.0b013e31821cbcc9>
- [10] *TLVs and BEIs Based on the Documentation Threshold Limit Values for Chemical Substances and Physical Agents and Biological Exposure Indices*. American Conference of Governmental Industrial Hygienists, 2022.
- [11] Otokpa O. E., Usman Y. B.: *An assessment of ultraviolet radiation components of light emitted from electric arc and their possible exposure risks*. Global Journal of Pure and Applied Sciences, 19/2. (2013) 145–149.
<https://www.ajol.info/index.php/gjpas/article/view/118658>

Comparison of Tool Steels for Tube End Flanging

Bence TRAUTMAN,¹ László TÓTH,² Enikő Réka FÁBIÁN³

¹ Óbuda University, Bánki Donát Faculty of Mechanical and Safety Engineering, Institute of Materials and Manufacturing Sciences, Budapest, Hungary, bencetrautman1@gmail.com

² Óbuda University, Bánki Donát Faculty of Mechanical and Safety Engineering, Institute of Materials and Manufacturing Sciences, Budapest, Hungary, toth.laszlo@bgk.uni-obuda.hu

³ Óbuda University, Bánki Donát Faculty of Mechanical and Safety Engineering, Institute of Materials and Manufacturing Sciences, Budapest, Hungary, fabian.reka@bgk.uni-obuda.hu

Abstract

One of the most important components of a tube end flaring machine is the flanging tool, which is subjected to mechanical stresses such as compression, bending and abrasion. It is therefore very important to choose the optimal material and manufacturing technology for the flanging tool. Böhler tool steel grades K110 and K340 were chosen as the subject of our research. Both materials were used to produce tube flanging tools, which were subjected to hardness testing, microscopic examination and surface wear testing after simple cooling or deep cooling and triple high temperature tempering after austenitisation in a vacuum at elevated temperature. Based on the measurements, the deep cooled and triple tempered K340 steel was found to be the most favourable tool steel for the production of the tube flanging tool.

Keywords: *tool steel, tube flanging, heat treatment, wear resistance, microstructure*

1. Introduction

The pipe flange used today has a long history. With the advent of new manufacturing technologies, many previously known manufacturing methods have been superseded (e.g. blind flanges and threaded flanges) and, as in all other areas, the need for standardisation to ensure interchangeability has developed. Flanges are used to connect equipment (pumps, valves, etc.) or additional pipes to the pipelines, and they also facilitate access to the pipes for subsequent installation or repair, if a repair is required within the system. This design is required where equipment and piping operating under high pressure is planned. A profitable tool is needed to make the flanges, as the wide range of uses of the technology means that it must be mass-produced in a cost-effective way, without compromising the tool's lifetime.

Another argument against welding is the knowledge that the welded joint environment can easily and often quickly corrode [1–3], and that the grain size in the heat-affected zone can become

coarse during welding, leading to a deterioration of the mechanical properties of the material [4]. The desire to prevent this, particularly in the interests of safety and sustainability, has become a fundamental principle.

In view of this, and in response to a constant assessment of market needs, the T-Drill company, which has been known since the 1960s for its pipe-machining machines and their manufacture, developed the cold-forming deep-drawing method. Modern cold-forming flanging technology is a technical process that reduces production time and costs by more than 40% compared to traditional welding.

This technology reduces the need for welding to a minimum and at the same time represents a qualitative leap, especially for systems used in the food industry, as the medium transported in the pipeline no longer encounters the weld root containing contaminants and the quality achieved meets hygiene requirements.

In the light of this achievement, the question arose: how could the flange of the pipes be designed in a different way? In answering this

question, T-Drill has created a major technological innovation, but its primary task was to flange light metals. The innovation was suitable as long as small diameters and low pressures had to be dealt with, but at the same time it became necessary to carry out further research and development into ways of flanging steel tubes that could cope with larger diameters and pressures.

This has led to the development of the technology that is now known and used worldwide: cold-formed pipe flanging. An essential tool and instrument for this is the tube flanging machine, of which the Tube flanging tool is an important part (**Figure 1**).

When using a flanging tool, it is subjected to compressive, abrasive and bending stresses, which reduce the tool life and thus increase the frequency of tool changes. This not only means the need for more flanging tools, but also poses a challenge for tool manufacturers. With these features in mind, Böhler K110 and K340 tool steels were chosen.

Both steel grades are ideal in terms of performance and price/value ratio, but heat treatments significantly affect the grain structure [5, 6] and thus the wear behaviour [7, 8]. of the steels. Gavriljuk et al [9] investigated the effect of cryogenic treatment on the martensitic transformation, Das et al [10] studied the carbide precipitation in similar cold forming tool steels. Other researchers [11, 12] dealt with changes in mechanical properties, and others [13, 14] with the effect of cryogenic treatment on wear properties. For our investigations, we first applied high temperature hardening and triple high temperature tempering on K110 and K340 materials, and then we also investigated K340 material grade specimens after high temperature hardening, deep cooling and triple high temperature tempering. Our tests were Rockwell hardness, abrasion, Charpy impact test and light microscopy studies for microstructure.



Figure 1. Tube flanging tool.

2. Materials, tools and technologies

K110 is a high carbon and chromium cold forming tool steel with good toughness and, due to the presence of carbide formers, excellent wear resistance. It is a recommended raw material for cold forming tools. Böhler grade K110 has EN number 1.2379, EN symbol X153CrMoV12, AISI symbol D2.

K340 Isodur is a universal cold forming tool steel grade with good compressive strength, wear resistance, excellent toughness and low dimensional change during heat treatment. It is produced by electroslag remelting and therefore has high purity and a favourable solidification structure. This steel has a low level of non-metallic inclusions due to its production technology. We have chosen these grades because their achievable properties meet the requirements of our tool material [4] The composition of our test specimens from K110 and K340 materials is presented in **Table 1**.

The hardness of the materials measured in their transport state ranged from 210 to 220 HB, so they are highly machinable. Our bar materials were turned into flanging tools - being a rotationally symmetrical product-. For heat treatment, we used a vacuum furnace type IU72/1F 2RV 60x60x40 10 bar CP Schmetz with an operating temperature range from -150°C to 1300°C, which was used for hardening, deep cooling and tempering (**Figure 2**).

Two different heat treatment technologies were used for grade K340. In the first case, high temperature (1060°C) quenching was followed by triple high temperature tempering (545, 555,

Table 1. Chemical composition of K110 and K340 steels

	C	Si	Mn	Cr	Mo	V
K110	1.55	0.30	0.30	11.30	0.75	0.75
K340	1.10	0.90	0.40	8.30	2.1	0.5

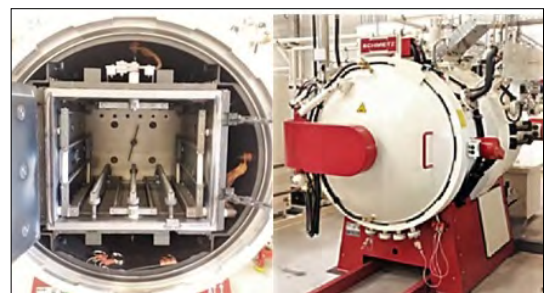


Figure 2. Vacuum heat treatment furnace.

535 °C), in the second case, after high temperature austenitisation, (1060°C), deep cooling with liquid nitrogen (-150°C) was followed by triple high temperature tempering (545, 555, 535 °C). Deep-cooling was chosen because it is a method to reduce the amount of residual austenite, to almost zero. The residual austenite would have a detrimental effect on the material by causing inhomogeneity and stresses. The heat treatment of the sample made by deep cooling was carried out as follows (Figure 3).

The heat treatment process for K110 tool steel is illustrated in Figure 4.

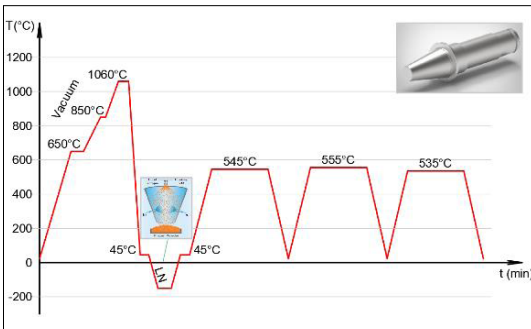


Figure 3. Cryogenic heat treatment diagram for K340 steel.

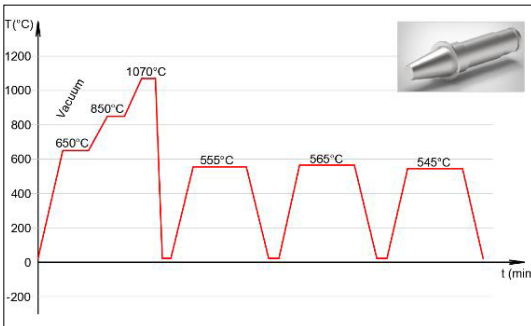


Figure 4. Heat treatment diagram for K110 steel.



Figure 5. Abrasive equipment.

3. Measurements and tests

After the heat treatments, hardness measurements were taken using an Ernst AT-130 hardness measuring machine. Then the tools were ground to the correct size. The specimens for the tests were machined into samples for the abrasion test. A picture of the abrasion apparatus is shown in Figure 5.

Ceramic balls with 20 mm diameter aluminium oxide based polished surface were used for the test. The duration of the measurements was 10 minutes and the speed was 570 rot/min in all cases..

The diameters of the abraded impressions were measured using an Olympus DSX1000 microscope. The image below shows a light microscope image of an abraded specimen (Figure 6).

The wear coefficient (K) was taken as a measure of wear, and can be calculated from the load force (N), wear volume (V_v) and wear path length (S). The calculations are based on the following formulae.

$$K = \frac{V_v}{S \cdot N}, \tag{1}$$

Where the wear volume can be derived from the depth of the spherical glass (h) and the diameter of the wear mark.

$$V_v = \frac{h \cdot \pi}{6} \left(\frac{3}{4} d^2 + h^2 \right), (mm^3) \tag{2}$$

The resulting spherical glass depth is calculated from the abrasive ball radius (R) and the diameter of the abrasion impression ($d = 2R$).

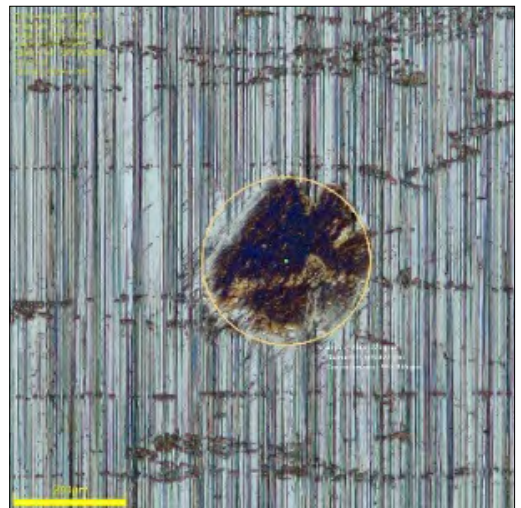


Figure 6. Abraded print

$$h = R - \sqrt{R^2 - \left(\frac{d}{2}\right)^2}, \quad (\text{mm}) \quad (3)$$

In addition, the wear path length can be determined by the radius of the abrasive sphere and its rotational speed (n):

$$S = 2 \cdot \pi \cdot n \cdot R \cdot t, (\text{m}) \quad (4)$$

In preparation for further microstructure studies, the samples were embedded in resin, polished, polished and etched with 2% Nital and examined under a Neophot 2 microscope.

The hardness measurement results and the obtained wear factors are summarised in **Table 2**.

The wear factors of samples with different heat treatments are illustrated in **Figure 7**.

The measured values show that the most abrasion resistant sample was the deep cooled and tiple tempered K340 grade steel, as confirmed by the microstructure.

The wear is presumably related to the microstructure. To investigate the microstructure, the samples were embedded in resin, sanded, polished and etched with 2% Nital and examined under a Neophot 2 microscope.

Since Nital does not etch carbides and austenite, the appearance of carbides in the samples, their distribution and the characteristics of the matrix surrounding the carbides could be examined at different magnifications.

Examining the samples at relatively low magnification, K110 steel shows a carbide network structure (**Figure 8**), whereas K340 grade is so typical because this steel was produced by electroslag remelting.

In each of these materials, typically slightly larger fragmented carbides are seen in the original grain boundaries (Figure 8), while in the matrix the carbides are much finer and more coarse-grained. For all steels the grain size is around 20 μm .

In the matrix of the K110 steel, fine spherical carbides are visible in addition to the stick-like carbides, while in the matrix of K340 steel the appearance of carbides are typically spherical (**Figure 9**).

In the light microscopy studies, it was found that when the K340 steel sample was austenitized at 1060°C, cooled under conventional conditions and then strained three times, residual austenite was still present in the fine structure matrix, whereas when the systematisation was followed by deep cooling and then the three times strain hardening at 1000x magnification, no residual austenite was

Table 2. Measurement results

Sample	Hardness HRC	Wear index (K) (mm ³ /Nm)
K110	60	05.00E-08
K340	59	04.49E-08
K340 deep cooled	60	04.40E-08

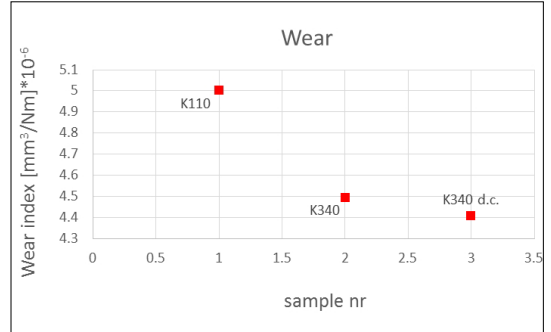


Figure 7. Wear factors of the tested samples.

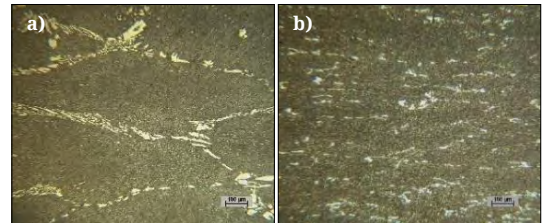


Figure 8. The appearance of carbide. Nital2%, N=100x, a) K110, b) K340.

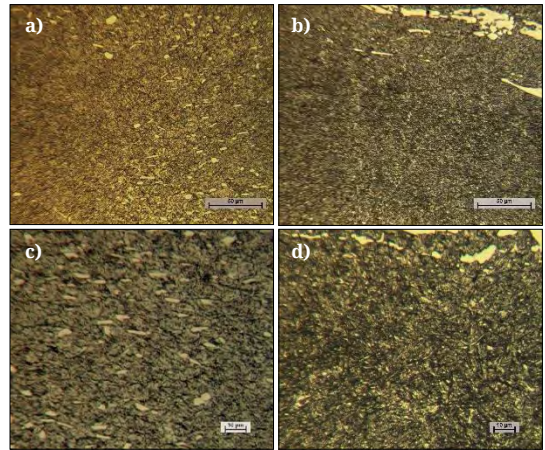


Figure 9. The matrix characteristics after usual heat treatments of the studied steels Nital 2%, a) K110 N=500x b) K340 N=500x c) K110, N=1000x d) K340 N=1000x

detected (Figure 10). In the photos carbide are spheric, the austenite appear between tempered martensite- (no spheric).

4. Conclusion

K110 is a good material grade, with good wear properties and hardness value, however microscopic tissue structure analysis demonstrates that it has a carbide reticulated structure, whereas this is not the case for the remelted material. In the K340 steel, the electroslag remelting results in a more homogeneous, finer and more uniform carbide distribution in the microstructure. In the microstructure of the K340 deep-cooled sample, residual austenite is typically not found, so no dimensional change after heat treatment is assumed in our sample and its lifetime is expected to exceed that of the previous two samples. The best resistance to wear of the deep-hardened and triple-strengthened K340 steel is due to the homo-

geneous carbide distribution and the fully transformed grain structure. Thus, the high temperature hardened, deep hardened and triple high temperature tempered K340 tool steel seems to be the most suitable material for the pipe milling tool of our choice. It is hoped that practical experience will bear this out.

Acknowledgements

This work was supported by the Hungarian State, National Research, Development and Innovation Office under the 2019-2.1.11-TÉT-2019-00093 number project. The authors would like to also thank the Hungarian State, the National Research, Development and Innovation Office and the European Union for their support in project No. 2020-1.1.2-PIA-CI-KFI-2020-00081.

References

- [1] Fábíán E. R., Kuti J., Gáti J., Tóth L.: *Corrosion Behavior of Welded Joints in Different Stainless Steels*. Revista De Chimie, 2020. 440–449. <https://doi.org/10.37358/RC.20.3.8018>
- [2] Kovács T., Pinke P., Széll K.: *Vékony lemezek hegesztés technológiájának tervezése/Welding Processes Specification of thin Sheets*. Abstracts Book of 10th International Engineering Symposium at Bánki, 2018. 51.
- [3] Dadfar M., Fathi M.H., Karimzadeh F., Dadfar M. R., Saatchi A.: *Effect of TIG welding on corrosion behavior of 316L stainless steel*. Materials Letters, 61. (2007) 2343–2346.
- [4] Kovács-Coskun T., Pinke P., Bitay E.: *A szemcseméret és a mechanikai tulajdonságok kapcsolatának vizsgálata hegesztett varratoknál*. Műszaki Tudományos Közlemények, 1. (2014) 125–130. <https://doi.org/10.33895/mtk-2014.01.11>
- [5] Tóth L., Fábíán E. R., Huszák Cs.: *Heat treatment Effects on Properties of K110 Böhler Steel*. Abstracts Book of 10th International Engineering Symposium at Bánki, 2018. 85.
- [6] Tóth L., Uri Szabó D.: *A mélyhűtés hatásai a szerszámacélok tulajdonságaira/The effects of the cryogenic treatment on the tool steel properties*. XXIX. Hőkezelés és Anyagtudomány a gépgyártásban Konferencia, 2020. 1–7.
- [7] Fábíán E. R., Tóth L., Huszák Cs.: *Examination of Heat Treatment on the Microstructure and Wear of Tool Steels*. Acta Materialia Transylvanica, 2/2. (2019) 87–92. <https://doi.org/10.33924/amt-2019-02-04>
- [8] Kovács T. A., Mhatre U., Nyikes Z., Bitay E.: *Surface Modification Innovation for Wear Resistance Increasing*. Iop Conference Series: Materials Science and Engineering, (2019) 613. <https://doi.org/10.1088/1757-899X/613/1/012039>

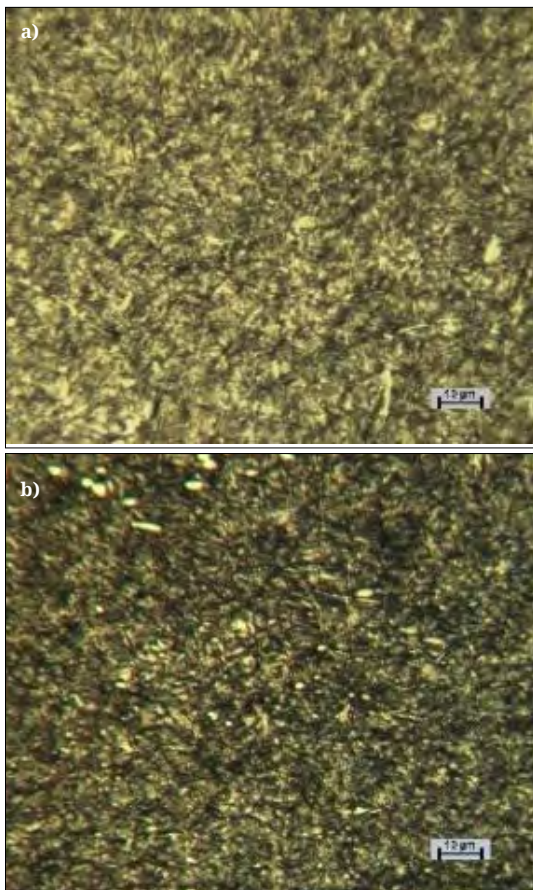


Figure 10. Residual austenite in the steels K340
a) conventional heat-treated sample,
b) deep cooled.

- [9] Gavriljuk V. G., Theisen W., Sirosh V. V.: *Low-temperature martensitic transformation in tool steels in relation to their deep cryogenic treatment*. Acta Materialia, 61. (2013) 1705–1715.
<https://doi.org/10.1016/j.actamat.2012.11.045>
- [10] Das D., Dutta A. K., Toppo V., Ray K. K.: *Effect of deep cryogenic treatment on the carbide precipitation and tribological behaviour of D2 steel*. Materials Manufacturing Process, 22. (2007) 474–480.
<https://doi.org/10.1080/10426910701235934>
- [11] Molinari A., Pellizzari M., Gialanella S., Straffellini G., Stiasny K. H.: *Effect of deep cryogenic treatment on the mechanical properties of tool steels*. Journal of Materials Processing Technology, 118/1–3. (2001) 350–355.
[https://doi.org/10.1016/s0924-0136\(01\)00973-6](https://doi.org/10.1016/s0924-0136(01)00973-6)
- [12] Das D., Sarkar R., Dutta A. K., Ray K. K.: *Influence of sub-zero treatments on fracture toughness of AISI D2 steel*. Materials Science and Engineering A, 528/2. (2010) 589–603.
<https://doi.org/10.1016/j.msea.2010.09.057>
- [13] Das D., Dutta A. K., Ray K. K.: *Sub-zero treatments of AISI D2 steel: part II. Wear behavior*. Materials Science and Engineering A, 527/9. (2010) 2194–2206.
<https://doi.org/10.1016/j.msea.2009.10.071>
- [14] Kumar S.; Nagaraj M., Khedkar N. K. , Bongale A: *Influence of deep cryogenic treatment on dry sliding wear behaviour of AISI D3 die steel*. Materials Research Express, 5/11. (2018) 116525, 1–9.
<https://doi.org/10.1088/2053-1591/aadeba>

Application-oriented use of Laser-induced Periodic Surface Structures

Márk WINDISCH,¹ Anna MALOVECZKY,² László ARADI,³ Miklós VERES,⁴ Péter FÜRJES,⁵ Ádám VIDA⁶

¹ Bay Zoltán Nonprofit Ltd. for Applied Research, Budapest, Hungary and Department of Materials Physics, Eötvös Loránd University, Budapest, Hungary, mark.windisch@bayzoltan.hu

² Bay Zoltán Nonprofit Ltd. for Applied Research, Budapest, Hungary, anna.maloveczky@bayzoltan.hu

³ Eötvös Loránd University, Faculty of Science, Research and Industrial Relations Center, Lithosphere Fluid Research Lab, aradi.laszloelod@ttk.elte.hu

⁴ Institute for Solid State Physics and Optics, Wigner Research Centre for Physics, Budapest, Hungary, veres.miklos@wigner.hu

⁵ Microsystems Laboratory, Centre for Energy Research, Budapest, Hungary, furjes@ek-cer.hu

⁶ Bay Zoltán Nonprofit Ltd. for Applied Research, Budapest, Hungary, adam.vida@bayzoltan.hu

Abstract

This paper investigates the phenomenon of Laser-induced Periodic Surface Structures (LIPSS) on Si single crystals. As usual, by variation of parameters, the morphological and physical properties of the resulting surfaces can be tailored, with respect to their use in many applications. One application-oriented use of LIPSS is the preparation of SERS (Surface Enhanced Raman Spectroscopy) substrates, which can be used to detect extremely low concentrations of molecules. In this experimental work, a possible way of manufacturing of SERS substrates, followed by SERS enhancement testing has been shown.

Keywords: LIPSS, Raman scattering, femtosecond laser, surface treatment, SERS enhancement.

1. Introduction

1.1. About LIPSS

The micro- and nano-meter periodic surface structures are created by laser surface treatment - LIPSS (Laser-induced Periodic Surface Structures) [1]. The LIPSS are created on metals, semiconductors and insulators. Morphological changes are formed as a result of the laser-material interaction by continuous and pulsed laser beam irradiation. The physical properties of the formed LIPSS are influenced by several parameters of the laser irradiation, such as the wavelength of the laser beam, irradiated energy density, pulse width and energy. In addition to the irradiation conditions, the properties of the created LIPSS can be significantly influenced by the free electron density, initial surface roughness and material structure of the irradiated material, as well as

the physical and chemical properties of the used medium [2].

The formed LIPSS have different mechanical and optical properties according to their modified surface and material structure properties and as a result they can be used in many different industrial applications. A possible tribological application of LIPSS is the controlled modification of wear properties of different steel surfaces, which can increase the service life of micro-components [3]. Another possible application field of LIPSS is the optical grid, which can be used to modify the optical properties of the elements of equipment for the semiconductor industry [4]. A biomedical application of LIPSS is the surface structuring of titanium-based implants. The LIPSS-covered surface provides the adhesion and growth of cells, so the integration can be accelerated, and the lifespan can also be increased [5].

Another possible application field of LIPSS are the formation of SERS substrates used in surface-enhanced Raman spectroscopy. The plasmonic structured surface of the substrates results in a significant Raman signal amplification of the investigated molecules due to the localized plasmon resonance [6].

1.2. Surface-enhanced Raman spectroscopy

The SERS is a complementary measurement technique to Raman spectroscopy. During surface-enhanced Raman spectroscopic measurements, the molecule to be tested is adsorbed onto the SERS active surface followed by the examination of the Raman spectrum of the molecule. The explanation of SERS enhancement is described by a mechanism based on chemical and electromagnetic interaction. The chemical interaction only affects the amplification to a small extent, so the electromagnetic theory can be used. According to the electromagnetic mechanism, surface plasmons are excited as a result of the incoming laser light. This leads to an increase in the electric field strength between the surface particles, which significantly increases the intensity of the Raman scattering emitted by the molecules to be examined. Based on theory, the amplification of the Raman signals can be increased by optimizing the size and shape of the surface particles and the distance between them.

The SERS substrates can be fabricated by different production techniques. For instance, roughening the surface of a plasmonic material or coating of the structured base surface with a plasmonic material (gold or silver). The aim of the experimental work was to fabricate a SERS substrate using the latter technique [7].

2. Examination methods

During the experimental work polished 4-inch p-type Si (111) wafer was used as SERS substrate [7]. The laser surface treatment was performed with a Coherent Monaco Nd:YAG (1035 nm wavelength) femtosecond impulse width (277 fs) laser device equipped with a 254 mm focal length F-theta lens. The surface of the structured silicon was coated with a gold layer using an AJA Orion vacuum evaporator at a pressure of 10-9 Pa. The surface of the SERS substrates were examined with a 4th generation TESCAN VEGA scanning electron microscope. The SERS enhancement of the fabricated substrates were investigated with the commonly used aqueous solution of 4-aminothiophenol (4-ATP) as a standard probe. The

measurements were performed using a Horiba LabRAM HR800 Raman microspectroscopy with a 633 nm wavelength, 1 mW laser power. The Olympus BXM microscope at magnification x50 and numerical aperture 0.6 was used to focus the laser onto the surface.

3. Experimental work

3.1. Preparation of SERS substrate

The SERS manufacturing process was started by laser engraving the back side of the silicon wafer in order to achieve a final substrate size of 6×4 mm (Figure 1).

In order to make the subsequent chopping of the silicon wafer easier, the wobbling technique was used during laser beam irradiation, and to ensure adequate heat dissipation another silicon wafer, located below the target wafer, was used.

After the engraving of the silicon wafer, structured 2×2 mm areas were created in the centre of the polished side by femtosecond laser equipment (Figure 2).

The laser irradiation was carried out with 1 MHz repetition frequency, 6.6 μJ pulse energy, 10 mm/s scanning speed and threefold overlap at atmospheric pressure.

After the surface structuring, the silicon wafer was coated with 5 nm titanium adhesion layer and 80 nm gold plasmonic layer using a vacuum evaporator (Figure 3).

After the coating process, the silicon wafer was broken into 6×4 mm pieces using lens tissue.

3.2. Investigation of SERS enhancement

The SERS enhancement of the fabricated substrates was investigated using 4-aminothiophenol (4-ATP) solution by Raman spectrometer (Figure 4).

3 μL of the solution was dropped onto the active surface of the SERS substrates, and after the solvent evaporation, analysis was carried out.

Measurements were performed by diluting the initial $0,5 \cdot 10^{-2}$ M stock solution to three orders of magnitude. An evaluable spectrum was obtained up to a solution with a concentration of $0,5 \cdot 10^{-4}$ M (Figure 4). The most diluted $0,5 \cdot 10^{-5}$ M solution no longer provided the spectrum characteristic of 4-ATP.

After the evaporation of the solvent, an approximately 100×110 μm areas was mapped using 2 μm steps on the substrate dropped with 4-ATP stock solution ($0,5 \cdot 10^{-2}$ M).

The integrated intensity of the main band of Si

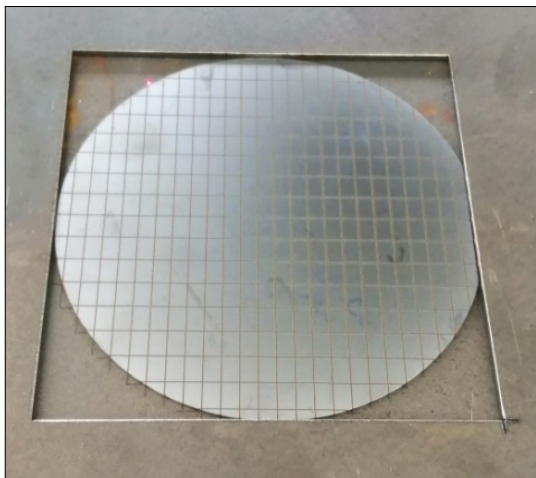


Figure 1. The back side of the silicon wafer after laser engraving

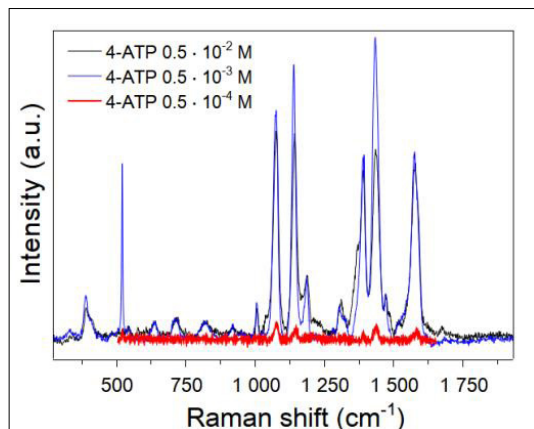


Figure 4. Raman spectra of 4-ATP solutions with different concentrations on the fabricated SERS substrate.



Figure 2. The surface of the silicon wafer during laser surface treatment.

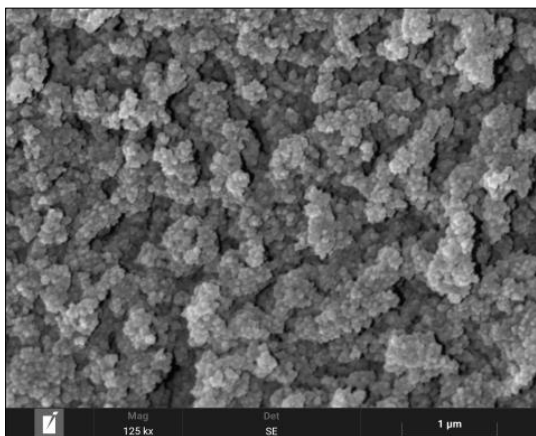


Figure 3. The structured surface of SERS substrate coated with gold.

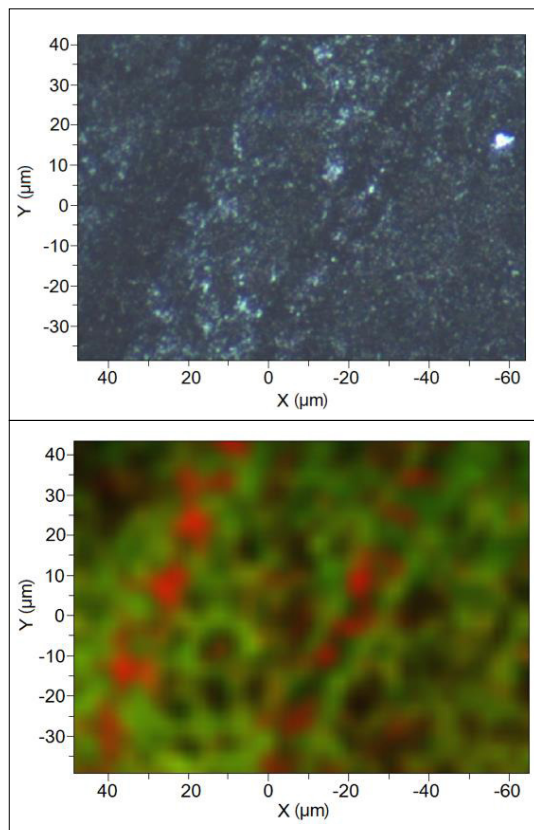


Figure 5. Raman mapping of the SERS substrate measured with 4-ATP stock solution: optical microscopic image of the examined area (figure above), map illustrating the Raman intensities of Si (red) and 4-ATP (green) signals (figure below).

(measured at 521 cm^{-1}) is marked in red, and the integrated intensity of the most intense bands of 4-ATP (between $1050\text{--}1600\text{ cm}^{-1}$) is marked in green in the map shown in Figure 5. There are two intensive diagonal lanes belonging to the band of Si. The amplifications of 4-ATP are appeared on the edge of ring-like spots with a diameter of $10\text{ }\mu\text{m}$ which can be referred to the morphological units repeating by laser beam overlapping.

Approximately 3.5–5 times (depending on the band) difference can be observed between the minimum and maximum intensities on the amplified bands of 4-ATP in Figure 6. The difference may be caused by the morphology of the substrate since the measurements were made in same focal plane during the mapping.

4. Product development

To further investigation of SERS enhancement of the substrate measurements were made with a 10^{-5} M Rhodamine 6G solution. During the same measurement conditions, the SERS enhancement of the fabricated substrate sensitivity was compared with commercially available SERS products [8].

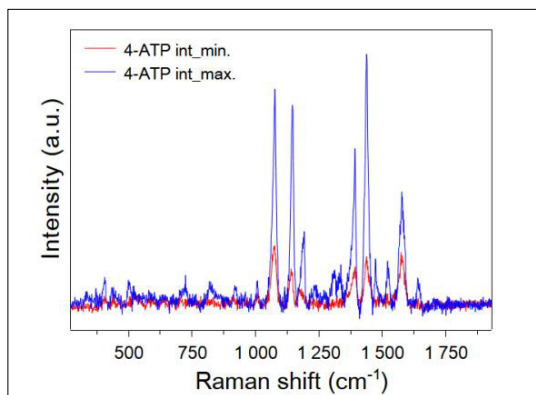


Figure 6. The minimum and maximum integrated spectra of the enhanced bands of 4-ATP in the Raman map are presented in Figure 5

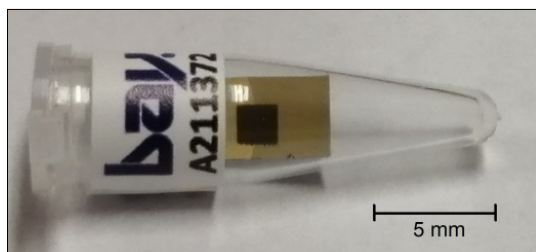


Figure 8. The fabricated SERS substrate.

The SERS enhancement of the fabricated substrate is within an order of magnitude comparable to the gold and silver-based SERS substrates of market leading companies (Figure 7).

Based on the promising results obtained during the investigation of the SERS enhancement product development was started.

The SERS substrates were put in a labelled PCR tube (Figure 8). The wrapped SERS substrates were placed in a vacuumed plastic bag and packed in a paper box with instructions for use (Figure 9).

5. Conclusions

There are many application-oriented uses of LIPPS. During the experimental work, we aimed to produce a SERS substrate applying surface-enhanced Raman spectroscopy with femtosecond pulse laser equipment.

The SERS enhancement investigation of the fabricated substrate was examined with 4-ATP and Rhodamine 6G molecule. During the Raman measurements, the amplification of the SERS substrate was compared with products available on the market. Based on the obtained results, the enhancement

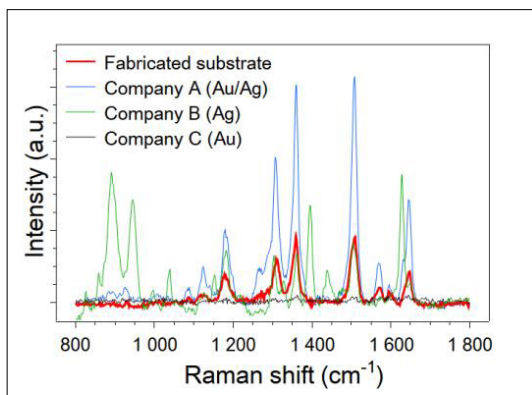


Figure 7. Comparison of the SERS enhancement of commercially available substrates.



Figure 9. The packed SERS substrates.

of the prepared SERS substrate approaches the sensitivity of market-leading products.

Based on the results, the SERS substrate product development has been started.

Acknowledgment

Project no. TKP2020-NKA-18 has been implemented with the support provided by the Ministry of Innovation and Technology of Hungary from the National Research, Development and Innovation Fund, financed under the 2020-4.1.1-TKP2020 funding scheme.

References

- [1] Van Driel H. M., Sipe J. E., Young J. F.: *Laser-induced periodic surface structure on solids: A universal phenomenon*. Physical Review Letters, 49. (1982) 1955–1958.
<https://doi.org/10.1103/PhysRevLett.49.1955>
- [2] Bonse J., Krüger J.: *Femtosecond laser-induced periodic surface structures*. Journal of Laser Applications, 24. (2012) 042006.
<https://doi.org/10.2351/1.4712658>
- [3] Bonse J., Koter R., Hartelt M., Spaltmann D., Pentzien S., Höhm S., Rosenfeld A., Krüger J.: *Tribological performance of femtosecond laser-induced periodic surface structures on titanium and a high toughness bearing steel*. Applied Surface Science, 336. (2015) 21–27.
<https://doi.org/10.1016/j.apsusc.2014.08.111>
- [4] Dusser B., Sagan Z., Soder H., Faure N., Colombier J. P., Jourlin M., Audouard E.: *Controlled nanostructures formation by ultra fast laser pulses for colour marking*. Optics Express, 18/3. (2010) 2913–2924.
<https://doi.org/10.1364/OE.18.002913>
- [5] Shinonaga T., Tsukamoto M., Kawa T., Chen P., Nagai A., Hanawa T.: *Formation of periodic nanostructures using a femtosecond laser to control cell spreading on titanium*. Applied Physics B, 119. (2015) 493–496.
<https://doi.org/10.1007/s00340-015-6082-4>
- [6] Bonse J., Höhm S., Kirner S. V., Rosenfeld A., Krüger J.: *Laser-Induced Periodic Surface Structures. A Scientific Evergreen*. IEEE Journal of Selected Topics in Quantum Electronics, 23/3. (2017)
<https://doi.org/10.1109/JSTQE.2016.2614183>
- [7] Le Ru E., Etchegoin P.: *Principles of Surface-Enhanced Raman Spectroscopy: and related plasmonic effects*. Elsevier, 2008.
- [8] Windisch M. és társai: *Femtosekundumos lézerrel Si egykristályon kialakított mikro- és nanostruktúrák vizsgálata*. Országos Anyagtudományi Konferencia poszter szekció rövid előadással, 2021.